

6

3772

3773

3774

Improved RPC investigation and preliminary electronics studies

3775 The extension in the endcap of the RPC sub-system towards higher pseudo-rapidity will bring the
3776 new detectors to be exposed to much more intense background radiations due to the proximity of
3777 the detectors with the beam line (Figure 4.5). The challenge will be to produce high counting rate
3778 detectors with limited ageing rate to ensure a stable operation of the detector over a period longer
3779 than ten years. In Chapter 3 was discussed the influence of the detector design (number and thickness
3780 of gas volumes, OR system, etc...) on the charge deposition and rate capability. Nevertheless, this
3781 question can also be addressed from the electronics point of view as a better signal-to-noise ratio
3782 would also mean the possibility to greatly lower the charge threshold on the signals to be detected,
3783 allowing to use the detector at lower gain, hence lowering the charge deposition per avalanche in the
3784 gas volume. Cardarelli showed that the production of low-noise fast FEEs could help decreasing the
3785 charge deposition per avalanche at working voltage by an order of magnitude, virtually increasing
3786 the life expectancy of such a detector in the same way [281].

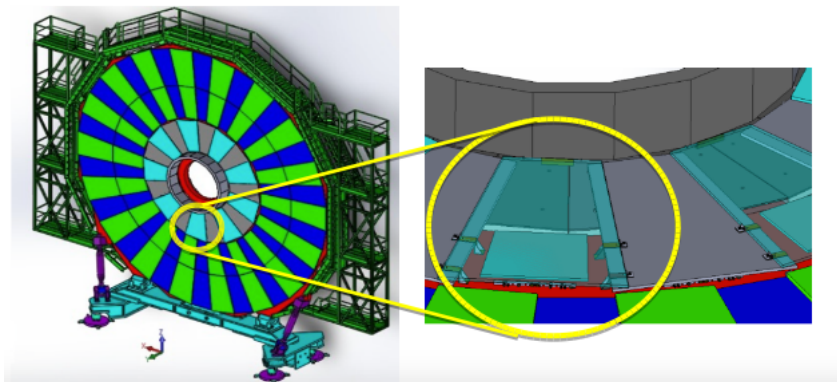
3787 In this Chapter will be presented the electronics that were chosen to equip the iRPCs that will
3788 installed on the CMS endcaps at the positions RE3/1 and RE4/1. These electronics are the CMS
3789 RPCROC. A similar technology has been previously used with RPCs in the context of the R&D of a
3790 Semi-Digital HCAL (SDHCAL) for the International Large Detector (ILD). As back-up to the CMS
3791 RPCROC, a FEB developed by the INFN Tor Vergata in Rome as also been studied for the CMS
3792 iRPCs.

3793 These two solutions for the iRPCs are the results of a longer selection process in which I took a great
3794 part. Thus, after an introduction of both technologies, the tests performed on CMS RPCs operated
3795 with preliminary versions of INFN Tor Vergata preamplifiers as well as with the HARDROC 2
3796 read-out panel of the SDHCAL will be discussed in details. Finally, the current status of the R&D
3797 certification will be presented. Nonetheless, it is important to keep in mind that I did not personally
3798 participate in the development of the CMS RPCROC nor of the INFN Tor Vergata FEB as designed
3799 for the iRPCs. My role was limited to the selection and to the test of potential candidates. After
3800 this preliminary study was conducted, the development of the actual FEEs for the CMS iRPCs was
3801 conducted by other researchers. Therefore, I will only report the status of the ongoing research.

3802 6.1 FEE candidates for the production of iRPCs

3803 The extension of the third and fourth endcap disks with improved RPCs has been presented in
 3804 Chapter 4 together with the expected background levels (Figure 4.18). The iRPCs will complete the
 3805 muon endcap as described in Figure 6.1. The key features of these iRPCs are:

- 3806 • double-gap design,
- 3807 • 1.4 mm thick HPL electrodes,
- 3808 • 1.4 mm thick gas gap,
- 3809 • trapezoidal chambers spanning 20° in φ around the beam axis,
- 3810 • read-out panel consisting of 96 trapezoidal strips
- 3811 • strip pitch ranges from 6.0 mm (5.9 mm) on the high pseudo-rapidity end to 12.3 mm (10.9 mm)
 3812 on the low one on position RE3/1 (RE4/1)
- 3813 • spatial resolution in the direction perpendicular to the strips ~ 3 mm



3814 *Figure 6.1: Location of the RE3/1 or RE4/1 iRPCs on a muon endcap disk.*

3815 An important piece of these iRPCs will be the Front-End Electronics that will equip the cham-
 3816 bers. A fast, low-jitter and low-charge sensitive electronics will help reducing further the charge
 3817 deposition in the detector by making it possible to operate at lower gain. The FEEs that are foreseen
 3818 to equip the new RPCs need to be able to detect charges as small as 10 fC. Not only the new elec-
 3819 tronics need to be fast and reliable, they also should be able to sustain the high radiation the detectors
 will be subjected to in the region closest to the beam.

3820 6.1.1 CMS RPCROC: the RPC upgrade baseline

3821 Designed by Weeroc, a spin-off company from the OMEGA Collaboration, the PETIROC 2A consists
 3822 in a fast and low jitter 32-channel ASIC originally developed to read-out Silicon Photomultiplier
 3823 (SiPM) in ToF applications and that allows for precise time measurements [257, 258]. The ASIC
 3824 uses an AMS 350 ns Silicon-Germanium (SiGe) technology. The block diagram of the ASIC is
 3825 showed on Figure 6.2. A 10-bit DAC allows to adjust the trigger level in a dynamical range spanning
 3826 from 0.5 to a few tens of photoelectrons and a 6-bit DAC to adjust the response of each individual
 3827 channel to similar a level.

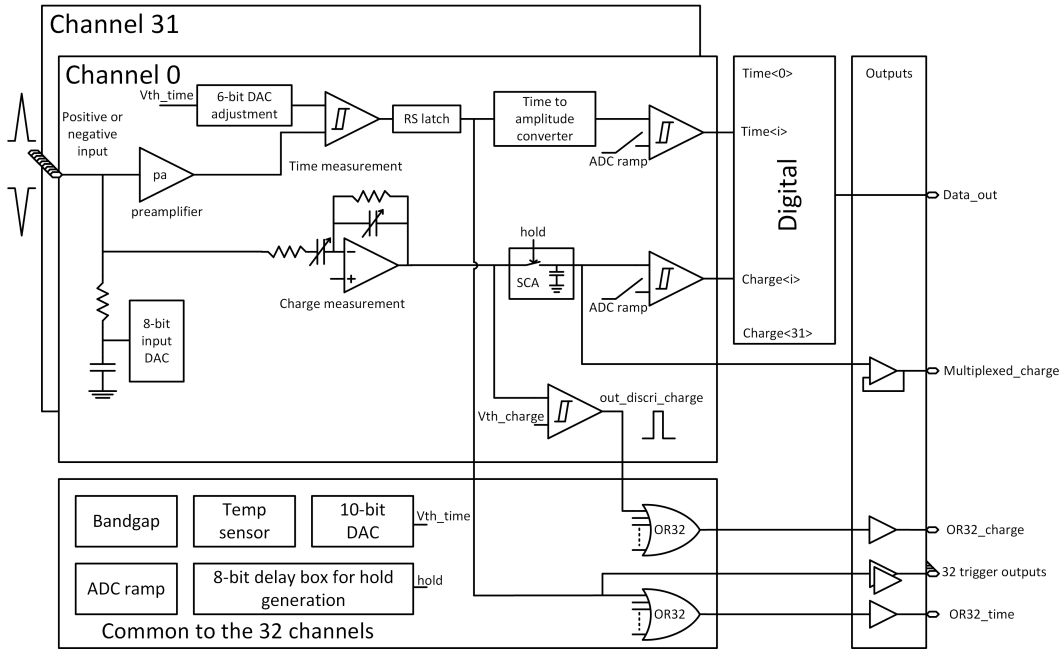


Figure 6.2: PETIROC 2A block diagram.

Nevertheless, to adapt this ASIC to CMS, modifications were brought to the PETIROC [177] and not all its functions will be used [282]. Due to the radiation levels that are foreseen at the level of the iRPCs, the SiGe technology will be replaced by the Taiwan Semiconductor Manufacturing Company (TSMC) 130 nm CMOS, to increase its radiation hardness while keeping fast pre-amplification and discrimination. On the Front-End Board, the ASIC is associated with an FPGA which purpose is to measure the arrival time of the signals. The FPGA is equipped with a TDC with a time resolution of 50-100 ps developed by Tsinghua University. The full system will provide a measurement of the signal position along the strip with a precision of a few cm by reading the signal on both strip ends. Finally, the measurement of the charge will be performed by a Time-over-Threshold (ToT) technic, taking profit of the capacity the ASIC in measuring both the leading and trailing edges of the input signals.

Two consecutive versions of the RPCROC are showed in Figure 6.4. FEBv0 was equipped with a single PETIROC 2A associated to a Cyclone II FPGA. FEBv1 was in turn equipped with two PETIROC 2A and then, in a later version, with two PETIROC 2B. In both cases, the ASICs were associated to a Cyclone V FPGA. The PETIROC 2B was a version of the ASIC with less cross-talk than the 2A. The dynamic range could then be expanded towards lower values to allow for the detection of charges as low as 50 fC. The next version, the FEBv2 is expected to be equipped with three PETIROC 2C, the new generation of the ASIC, associated to three Cyclone V FPGAs hosting the 32-channel TDCs and a master Cyclone V FPGA for the communications of the TDCs with the Link-Board system. The version 2C will focus on reducing the dead-time of 10 ns of the ASIC. Also, the Cyclone V FPGAs of the FEBv2 will use a different technology than the one used for FEBv1. The choice has been made to use a radiation tolerant PolarFire FPGA which uses data scrubbing to detect and correct errors before they accumulate. This technology is for example used for space applications. The FEB will be tested at the Louvain-la-Neuve (LLN) neutron beam. The goal is to irradiate the electronics up to a fluence of 10^{14} pC/cm^2 , five times more than what is expected at CMS, to certify its radiation hardness.

3854



Figure 6.3: (a) View of the RPCROC FEBv0 in which the PETIROC 2A ASIC is visible as well as the FPGA on which the TDC is hosted. (b) View of the RPCROC FEBv1 with its two PETIROC 2A ASICs. The FPGA with the TDC is this time embedded in the FEB.

3855

Each FEBv2 will be able to read 96 channels out thanks to three 32-channel PETIROC 2C ASICs. Two FEBv2 would be mounted on the iRPC to read the 96 strips out from both ends. The read-out panel that was used for the v1 of the RPCROC is shown in Figure 6.4a and the final design with the FEBv2 mounted on the read-out plane is shown in Figure 6.4b.

3856

3857

3858

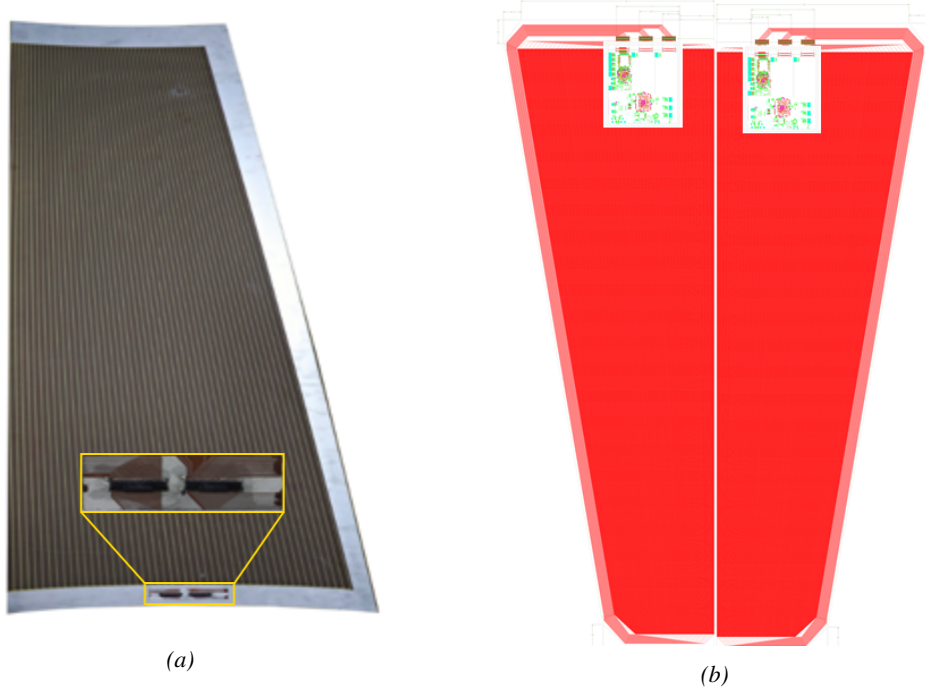


Figure 6.4: (a) Picture of half the read-out PCB used with FEBv1. The RPCROC is connected directly onto the return connectors on the wide end of the panel. (b) Design of the foreseen final read-out of the iRPC showing the 2 RPCROC FEBs and the read-out PCB.

3859 6.1.2 INFN FEB: a robust back-up solution

3860 Even though the baseline for the electronics that will equip the iRPCs will be the CMS RPCROC,
 3861 a back-up solution needs to be certified. The back-up has been found in Front-End Electronics
 3862 featuring a fast and low-noise ($1000 e^-$ rms) Silicon (Si) preamplifier and a SiGe discriminator [283]
 3863 associated with an optimized read-out panel [284]. The low-noise preamplifier is a new version of
 3864 a preliminary production of a SiGe preamplifier by the team of Cardarelli working with INFN Tor
 3865 Vergata in Rome with the purpose of equipping the new generation of ATLAS RPCs [285]. The
 3866 study of the early version of the preamplifier by is discussed in Section 6.2.

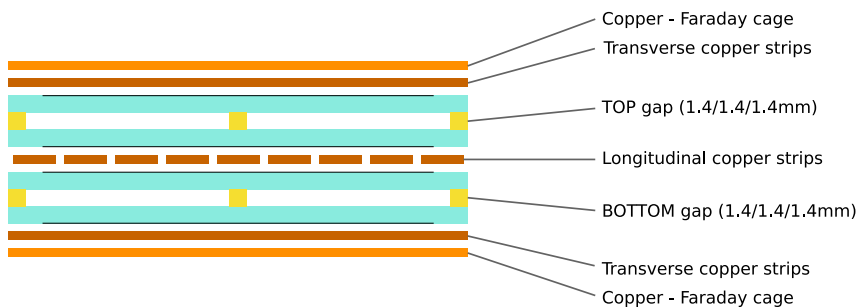


Figure 6.5: Design of the iRPC in the back-up scenario. The detector includes an additional two layers of transversal strips to gain in spatial resolution.

3867 Contrary to the CMS RPCROC, the back-up electronics only offer the possibility to read the
 3868 96 strips out from one end. The spatial resolution along the strips is then brought by two transverse
 3869 strip planes. These two additional panels sandwich the *gaps+strip* ensemble as showed in Figure 6.5.
 3870 They feature 5 cm wide copper strips for a spatial resolution of a few centimeters along the longitudi-
 3871 nal strips. A top quarter of the longitudinal and transversal read-out panels is shown in Figure 6.6
 3872 and pictures are available in Figure 6.7.

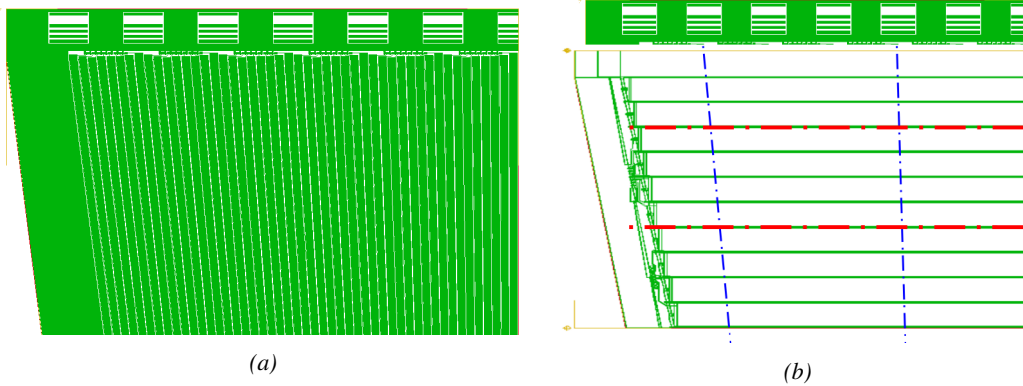


Figure 6.6: Design of the longitudinal (a) and transversal (b) strip panels. The transversal design is here shown on top of the longitudinal one.



Figure 6.7: Picture of half the longitudinal (a) and of the top part of the transversal (b) strip panels.

3873 The FEB used for the longitudinal readout is shown in Figure 6.8a. Each FEB is equipped
 3874 with eight preamplifiers using a Bipolar Junction Transistor (BJT) technology and two discrimina-
 3875 tor ASICs of four channels using Hetero Junction bipolar Transistor (HJT) technology. The input
 3876 signals are amplified at an amplification factor of 0.2 to 0.4 mV/fC and are then discriminated with
 3877 a threshold of 0.5 mV at minimum. For each channel, the LVDS output is proportional in width to
 3878 the Time-over-Threshold in the discriminator of the amplified signal with a minimum width of 3 ns.
 3879 This method allows for an estimation of the avalanche charge as the width of the signals usually is
 3880 consistent and proportionnal to the amount of charge released in the gas volume.
 3881 On Figure 6.6a, the rectangular zones with straight copper lines at the top of the longitudinal PCB
 3882 are lines used to propagate the power and the slow control of the FEBs. A FEB is placed between

3883 two zones and soldered to the copper lines on both sides, as can be seen in Figure 6.8b. in the same
 3884 way, the FEB is soldered to a group of eight strips which lines finish into pads placed below the
 3885 bottom edge of the FEB. It was decided to solder the FEBs onto the read-out PCB to reduce the
 3886 pick-up noise in the electronics.

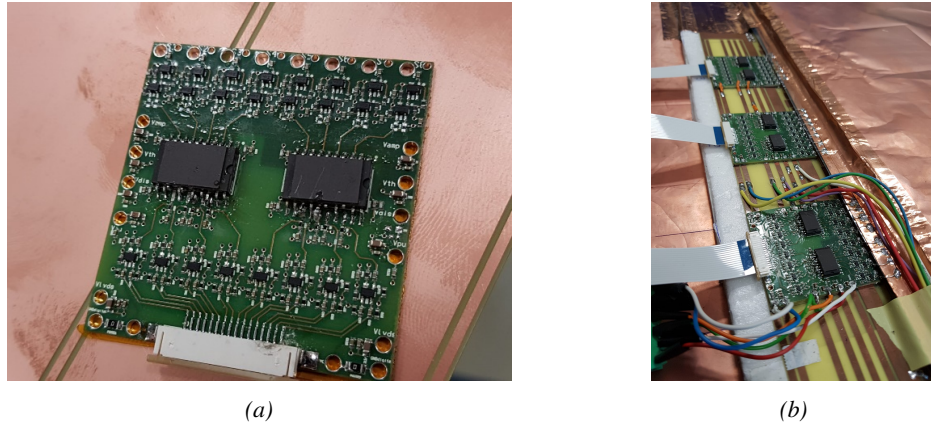


Figure 6.8: Version 2 of the INFN Tor Vergata FEB as designed for the CMS iRPC. The FEBs are directly soldered onto the read-out PCB to reduce pick-up noise as much as possible. Copper lines embedded into the PCB are used to propagate the power and slow control lines.

3887 The strips begin much wider in the case of the transversal read-out panel, the FEB design is a
 3888 little different, as can be seen in Figure 6.9a. The transversal FEBs are strictly the same as the one
 3889 attached to the longitudinal plane even though they are wider. AS of now, the connection of the
 3890 FEBs to the power and slow control lines is done via coaxial cables as can be seen from Figure 6.9b.
 3891 Only the connection to the strips was optimized for direct on-PCB soldering.

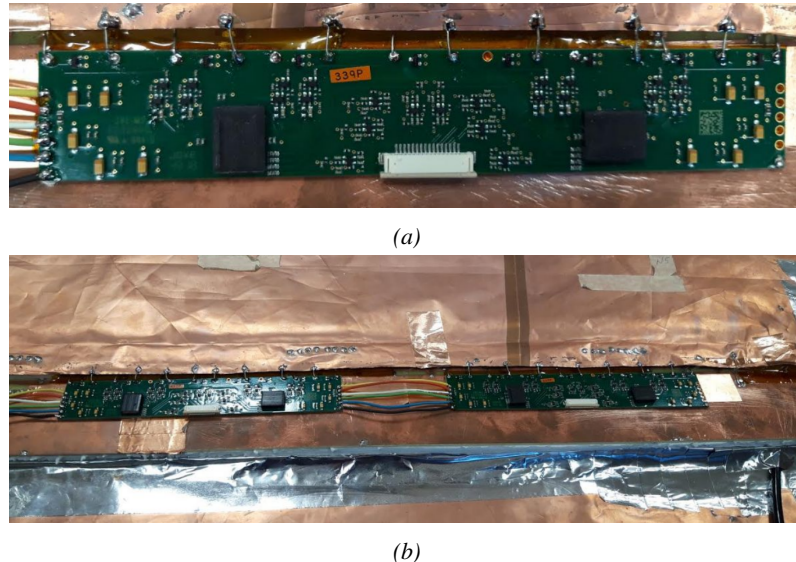
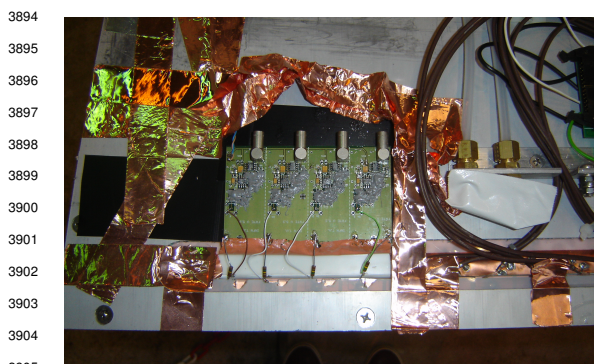


Figure 6.9: Version of the INFN Tor Vergata FEB as designed for the transversal readout panels of the CMS iRPC. The FEBs are directly soldered onto the read-out PCB to reduce pick-up noise as much as possible. The propagation of the power and slow control lines is done via coaxial cables.

3892 6.2 Preliminary electronics tests at CERN

3893 6.2.1 INFN preamplifiers as upgrade candidates



3894
3895
3896
3897
3898
3899
3900
3901
3902
3903
3904
3905
3906
3907
3908
3909
3910
3911
3912

Figure 6.10: The four channels of INFN preamplifiers are mounted directly on a CMS RPC and connected to the four outermost read-out strips of the detector.

INFN electronics were the first ones to be tested by CMS RPC group in collaboration with colleagues from INFN Roma working in the ATLAS RPC group. The tests with CMS RPCs were performed in February 2013 outside of the old GIF facility presented in Chapter 5.1.1. Four preamplifier channels were lended by Cardarelli to equip four CMS RPC channels as presented in Figure 6.13. They were directly connected to the strips for the signals induced by muons passing through the gas volume of the chamber to be amplified. The output was then sent to a discriminator to digitize the signals and filter out the noise by tuning the threshold level. The NIM quad discriminator 821 manufactured by LECROY

used during this experiment only allows at minimum to set the threshold at a voltage of approximately 30 mV on the input signals. Thus, two values of discrimination were used (~ 75 mV and ~ 30 mV).

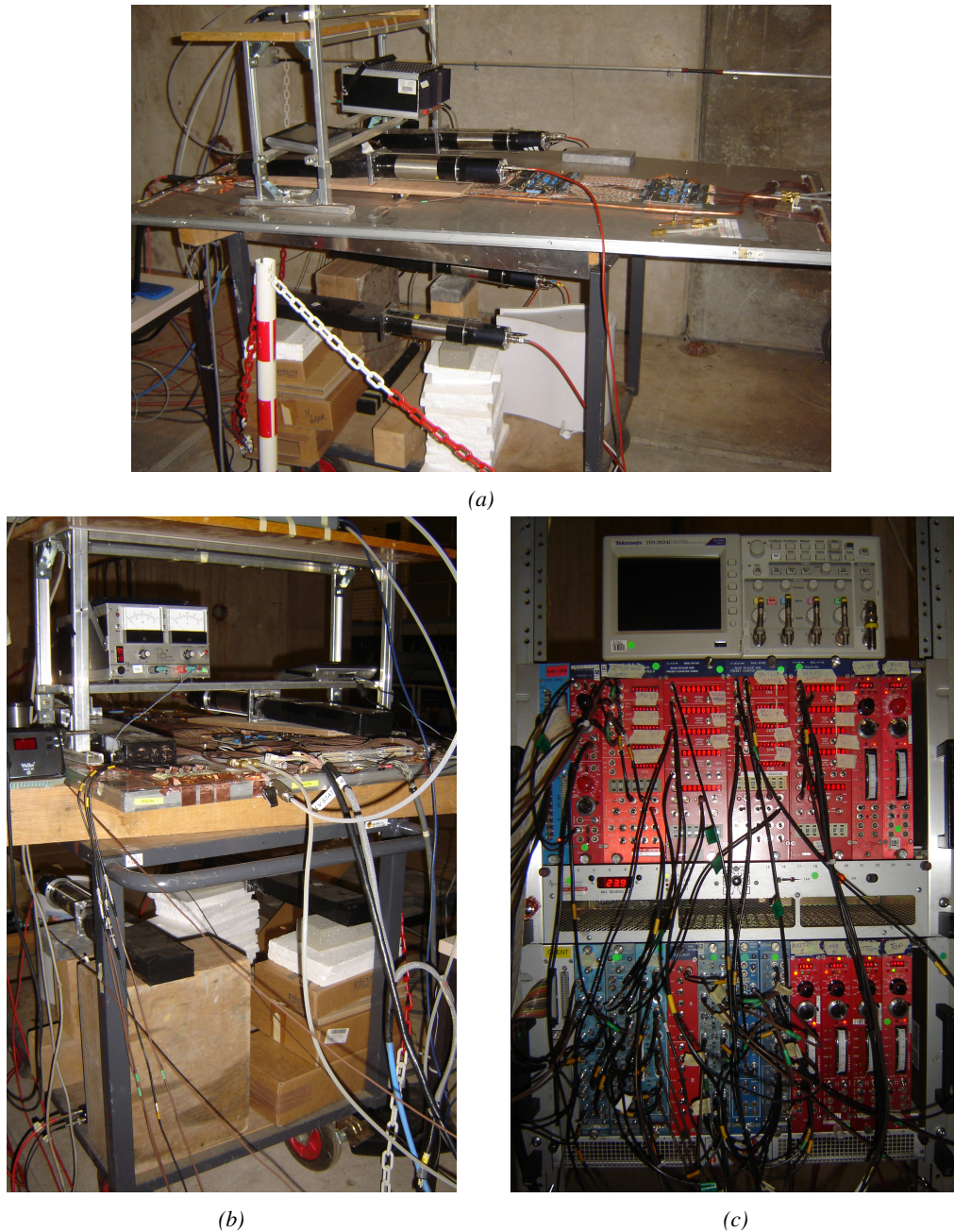


Figure 6.11: Experimental setup used to test the INFN preamplifier with respect to the CMS FEEs.

3913 The performance of the chamber equipped with these new preamplifiers was compared to the
 3914 performance of CMS FEEs. The experimental setup used is described in Figure 6.11. PMTs a little
 3915 less wide than four strips were used to trigger the data taking. Two pairs were used in coincidence
 3916 on both the strips connected to the INFN preamplifiers and to the ones connected to the CMS FEEs.
 3917 An extra PMT, placed perpendicularly to the rest of the setup at the bottom of the setup was used
 3918 to detect potential showers and send VETO signals if necessary. A last PMT was used close to the

power supplies to measure and discard signals due to electromagnetic noise and is not visible on the pictures. Finally, after discrimination, the output of the INFN preamplifiers together with the signals from the CMS FEEs were sent to scalers to count the detected signals versus the number of trigger coincidences as no DAQ software was available at the time. The full pulse processing for this experiment is shown in Figure 6.12.

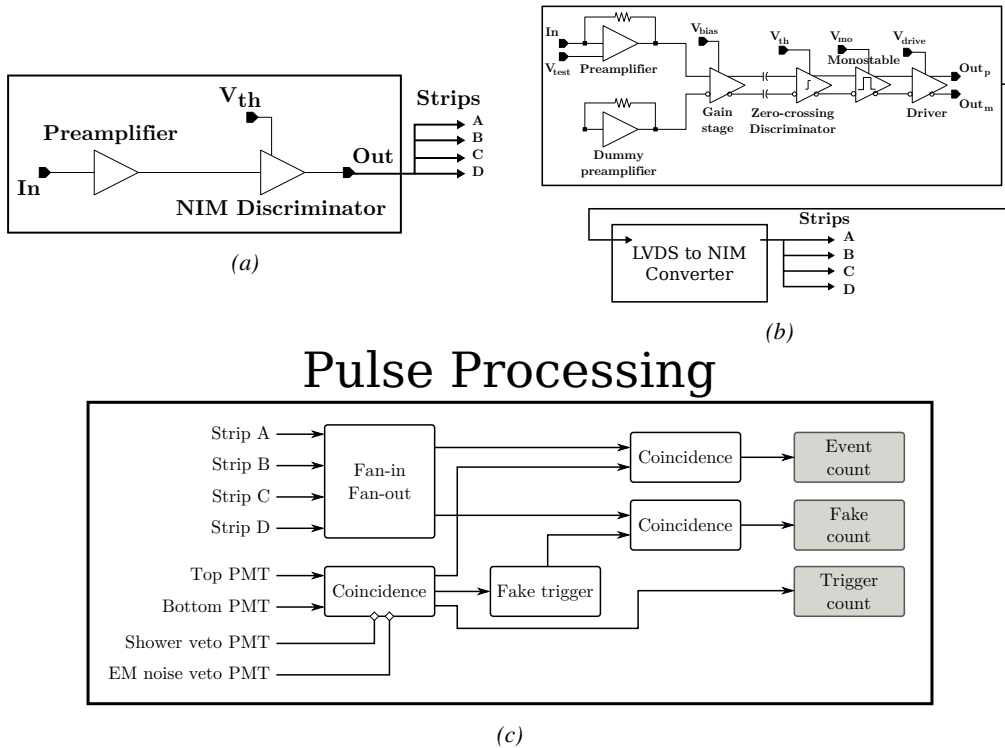


Figure 6.12: The block diagrams corresponding to the signal treatment for both INFN preamplifier (Figure 6.12a) and CMS FEEs (Figure 6.12b) are shown. The digitized signals are then counted in coincidence with the trigger signals provided by PMTs (Figure 6.12c).

The data taking program consisted in High Voltage scans. A first point was taken at 0 V to only measure noise. Then the HV was increased to an applied value of 7 kV. The voltage was increased in steps of 500 V until 8 kV from where it was increased in steps of 100 V until an upper limit of 10 kV. After rising the voltage over the electrodes of the RPC, a waiting period of 15 minutes was observed to leave time to the electrodes to charge and to the currents to stabilize. The currents were reported at the moment the data taking was started. At each HV step, except at 0 V, approximatively 300 triggers were taken to estimate the efficiency of the detector by counting the number of hits in the system (A or B or C or D), referring to the strips. The noise rate per unit area was measured during the first 100 s of data taking by counting the number of hits received in each read-out strip. The cluster size, the average number of adjacent strips fired during a muon event, could not be measured due to the lack of available scalers. During the data acquisition, in addition to counting the number of signals with respect to the number of triggers, the current or the noise rate per unit area as a function of the increasing voltage, the environmental parameters were monitored. Using the information provided by a humidity and temperature sensor on the gas input line together with the environmental pressure given by a weather station, the applied voltage could be corrected following Formula 3.27. Moreover, the voltage line

3940 was filtered to prevent noise and higher currents in the RPC under test.

3941 The results of the preliminary tests are presented in Figure 6.13. More details on the fit performed
 3942 on the data are provided in Table 6.1. As can be seen, being able to use electronics with a much
 3943 higher sensitivity allows for a HV shift of up to 475 V with a threshold as low as 3 fC corresponding
 3944 to the lowest threshold available on the discriminator modules. On the other hand, the higher charge
 3945 sensitivity also brings a higher noise level. After a first series of measurement performed with a bad
 3946 grounding leading to grounding loops and hence an artificially higher noise, it can be concluded that
 3947 the noise rate per unit area of such electronics is approximately one of manitude higher than the noise
 3948 rate measured with the CMS FEB. The noise reaches approximately 2 Hz/cm^2 at the level of the
 3949 working in the case of the INFN preamplifier while it is lower than 0.2 Hz/cm^2 for the CMS FEB.
 3950 It is likely that the higher sensitivity also brings a higher sensitivity to local discharges happening
 3951 in the gas due to fluctuations of the electric field. The surface of the electrodes not being perfectly
 3952 smooth, the local electric field may vary quickly. The gas molecules circulating in the gas could
 3953 then be ionised by the fast variation of the field and trigger an avalanche that can then be detected.
 3954 Reducing the noise rate per unit area would then come from an improvement of the detector itself
 3955 rather than from a reduction of the electronic noise of the INFN preamplifier.

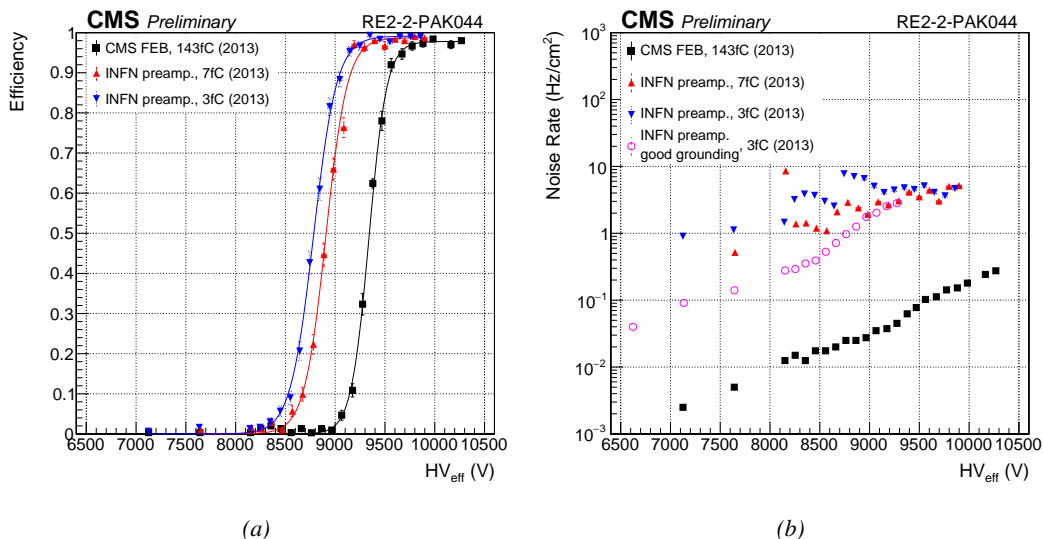


Figure 6.13: Efficiency (Figure 6.13a) and noise rate per unit area (Figure 6.13b) of the CMS RE2-2 detector tested with the standard CMS FEBs (black) and with the INFN preamplifier at different thresholds (red and blue). An extra HV scan was performed with better conditions to measure the noise with a threshold of 3 fC on the INFN preamplifiers.

Data	ϵ_{max}	$\lambda (\times 10^{-2} \text{ V}^{-1})$	$HV_{50} (\text{V})$	ϵ_{WP}	$HV_{WP} (\text{V})$
CMS FEB, 143fC (2013)	0.978 ± 0.004	1.12 ± 0.07	9339 ± 11	0.97 ± 0.01	9752 ± 27
INFN preamp., 7fC (2013)	0.987 ± 0.003	0.93 ± 0.05	8907 ± 11	0.97 ± 0.01	9374 ± 27
INFN preamp., 3fC (2013)	0.991 ± 0.003	0.86 ± 0.04	8783 ± 11	0.98 ± 0.01	9276 ± 27

Table 6.1: Results of the sigmoid fit (Formula 3.24) performed on the data presented in Figure 6.13a. The working point and its corresponding efficiency are computed using Formulas 3.24 and 3.25.

3956 6.2.2 INFN preamplifiers mounted onto CMS Front-End Board

3957 Following the first experiment performed in the experimental hall aside of the old GIF, a new se-
 3958 ries of tests has been done in the CMS RPC assembly laboratory at CERN. For this purpose, the
 3959 preamplifiers have been designed to be standalone single channels. To have a consistent comparison
 3960 with the CMS FEB, a FEB prototype has been built based on the current CMS design. As shown
 3961 in Figure 6.14, the preamplifiers are meant to be plugged in one of the available 16 channels of the
 3962 board that produces an LVDS output with similar characteristics than the CMS FEB.

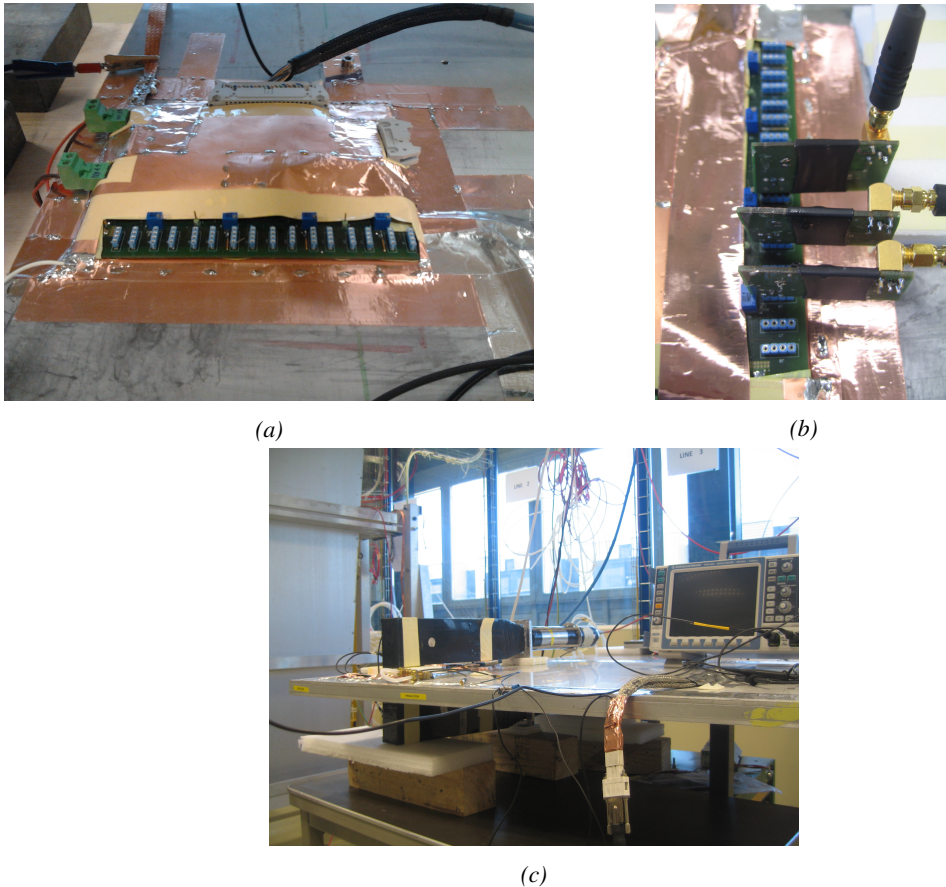


Figure 6.14: Figure reffig:Setup-INFN-904:A: Shielded Front-End Board on which the INFN preamplifiers are to be mounted. Figure reffig:Setup-INFN-904:B: Three INFN preamplifiers connected onto the test FEB. Figure reffig:Setup-INFN-904:C: Experimental setup used to test the INFN preamplifier single mounted on a FEB similar to the CMS FEB.

3963 At the time of the second experiment, only three channels could be lent by the team of INFN
 3964 Roma. The impedance of the preamplifiers was set to 100Ω at delivery. The strips are then con-
 3965 nected to the preamplifiers using 50Ω coaxial cables equipped with SMC connectors, known for
 3966 their good transmission. To match the impedance of the preamplifier input with the signal cable,
 3967 a 100Ω resistor was added in parallel of the input line. In CMS endcap RPCs, the strips are left
 3968 floating. For the purpose of this test, it was necessary to terminate the strips on both ends to prevent
 3969 reflections in the transmission line. The impedance of the strips being approximately 25Ω , the strips
 3970 were terminated with 50Ω resistors on the signal cable side, and with 25Ω resistors on the end side.

3971 The threshold of the zero-crossing discriminators used on the FEB is controled via a labview interface similar to the one used to control the threshold of the CMS FEB. Various thresholds were used
 3972 in a range in between 7 and 5 fC. These values are a little higher than the minimal threshold of about
 3973 3 fC used during the first experiment due to limitations of the FEB itself.

3974 Finally, it was decided to use the same PMTs than in the first experiment as trigger. This time, they
 3975 were placed on their narrow side to only cover an area on the detector smaller than three strips. On
 3976 the data acquisition side, no DAQ software was available yet at the time of experimentation and
 3977 scalers were once again used. As can be seen from Figure 6.15, the pulse processing has been in-
 3978 spired by the previous scheme. Thanks to the lower number of channels to monitor, the cluster size
 3979 could be estimated by counting the signals on single channels (A, B and C on their own) but also
 3980 on groups of two (A and B, B and C) and three channels (A and B and C) in coincidence with the
 3981 trigger.
 3982

Pulse Processing

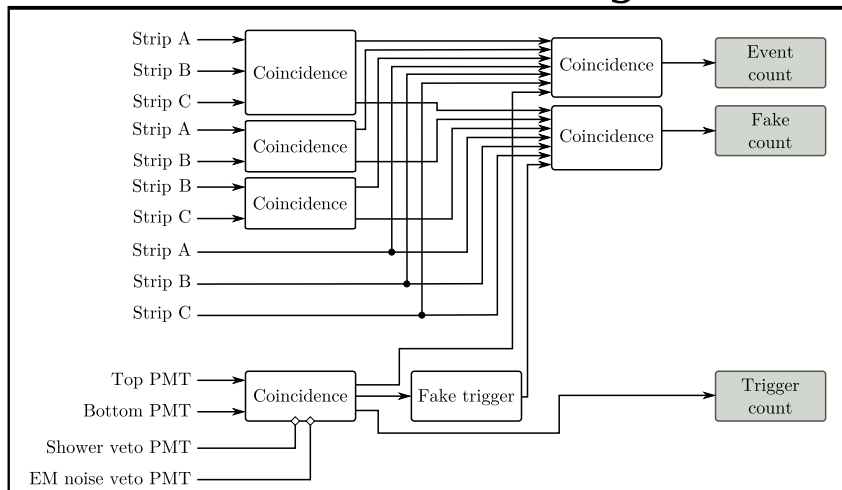


Figure 6.15: Similarly to Figure 6.12c, the signals are counted in coincidence with the trigger signals provided by PMTs. To estimate the cluster size, the channels are counted by groups of three, two but also alone.

3983 The results of the second round of tests with INFN preamplifiers are presented in Figure 6.16 and
 3984 Table 6.2. These results are consistent with what was measured with the first tested prototypes. The
 3985 efficiency sigmoid has been measured once again with the CMS FEB, using a threshold of 146 fC
 3986 and is in agreement with the data collected in 2013. The performance of the detector with the pream-
 3987 plifiers tuned at 7.2 and 6.4 fC falls in the very same values than the setting at 7 fC according to the
 3988 table. A maximum shift of 410 V is observed for a threshold of 5 fC.

3989 With the care placed into having a good grounding of the setup as well as a good impedance match-
 3990 ing, the noise rate per unit area is this time lower than what previously measured. Nevertheless, it
 3991 still is more than one order of magnitude higher than in the case of the CMS FEB with a threshold
 3992 set at 146 fC. The noise rate is measured to be at lowest around 0.7 Hz/cm^2 when measured to be
 3993 approximately 0.05 Hz/cm^2 for the CMS FEB. At such high threshold values, the noise rate per unit
 3994 area is not expected to vary much. The data collected at the RPC assembly laboratory then displays
 3995 much better data tacking conditions with both electronics.

3996 Finally, the cluster size is measured to be similar for both electronics at the level of the working
 3997 point and is in between 2.2 and 2.4 strips on average. The spatial resolution of both devices would
 3998 then be the same.

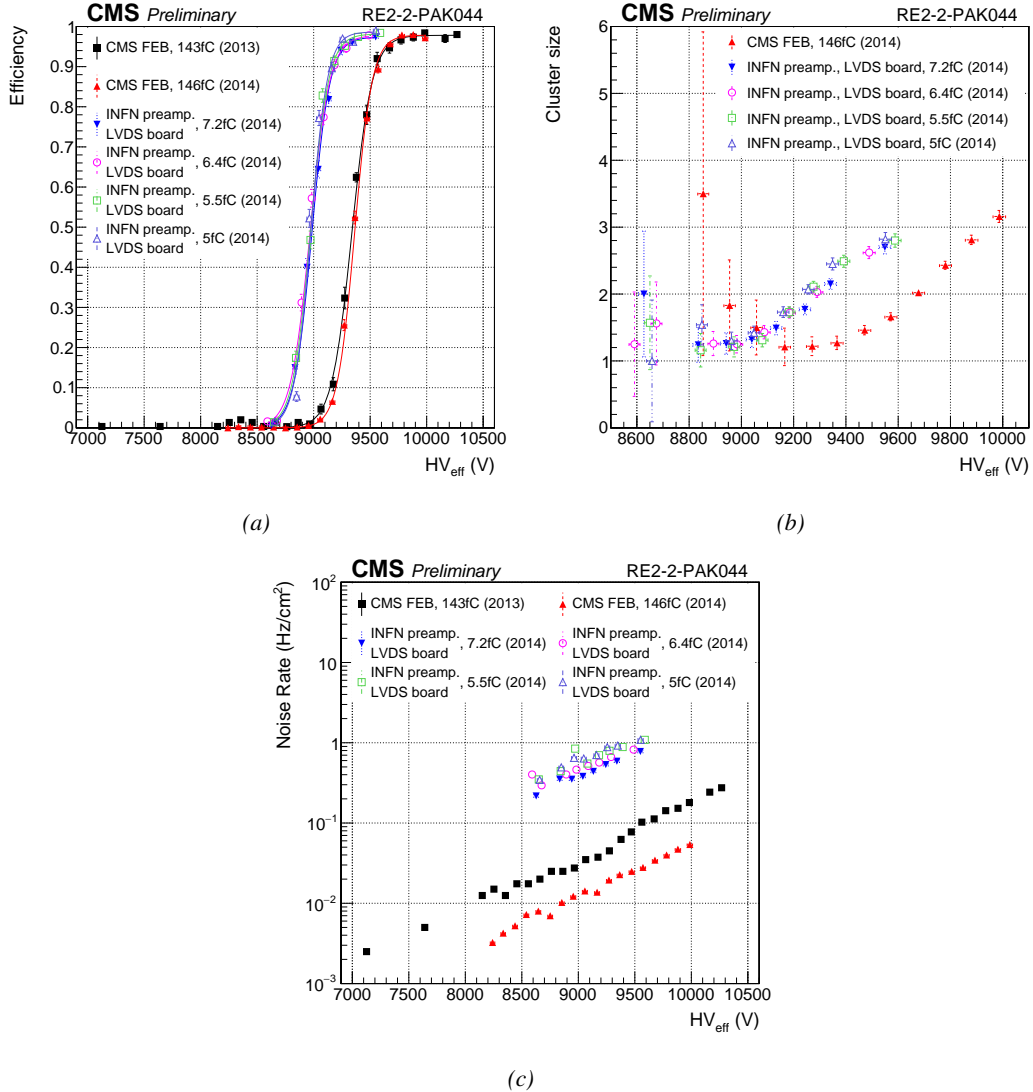


Figure 6.16: Efficiency (Figure 6.16a), cluster size (Figure 6.16b) and noise rate per unit area (Figure 6.16c) of the CMS RE2-2 detector tested with the standard CMS FEBs (black and red) and with the INFN preamplifier mounted onto the CMS FEB at different thresholds (blue, pink, green and purple).

Data	ϵ_{max}	$\lambda \cdot 10^{-2} \text{ V}^{-1}$	$HV_{50} (\text{V})$	ϵ_{WP}	$HV_{WP} (\text{V})$
CMS FEB, 143fC (2013)	0.978 ± 0.004	1.12 ± 0.07	9339 ± 11	0.97 ± 0.01	9752 ± 27
CMS FEB, 146fC (2014)	0.978 ± 0.003	1.30 ± 0.06	9364 ± 9	0.97 ± 0.01	9740 ± 19
INFN/CMS FEB, 7.2fC (2014)	0.973 ± 0.006	1.26 ± 0.09	8985 ± 10	0.97 ± 0.01	9368 ± 26
INFN/CMS FEB, 6.4fC (2014)	0.978 ± 0.007	1.16 ± 0.08	8969 ± 11	0.97 ± 0.01	9372 ± 28
INFN/CMS FEB, 5.5fC (2014)	0.981 ± 0.005	1.26 ± 0.09	8973 ± 12	0.97 ± 0.01	9357 ± 28
INFN/CMS FEB, 5fC (2014)	0.987 ± 0.004	1.37 ± 0.10	8976 ± 12	0.98 ± 0.01	9342 ± 28

Table 6.2: Results of the sigmoid fit (Formula 3.24) performed on the data presented in Figure 6.16a. The working point and its corresponding efficiency are computed using Formulas 3.24 and 3.25.

In addition to the tests performed on the electronics with the CMS RPC, the electronics also have been tested on a gRPC designed in Ghent. The gRPC used for this experiment is described in Figure 6.17. The detector, showed on Figure 6.18, uses a double-gap layout with float glass electrodes of 1.1 mm and a gas gap of 1.2 mm. The electrodes themselves are made out of four pieces of glass glued together. Such a design was studied for high-rate detection purposes and aimed to serve as a proof of concept for RPCs built using small pieces assembled together to produce a larger detection area. Indeed, in the context of R&D in the field of high-rate RPCs, most low resistivity materials are custom made doped glass or ceramics plates. These materials can't be produced in large areas as they are not manufactured on a large enough scale. Thus, building large detectors can imply using such methods.

The tests involving this detector were conducted in 2015 with the setup described by Figure 6.19. The photomultipliers used to trigger the data taking were a little larger than the detector and the strips themselves. Similarly to the case of the GIF experiment described in Section 5.2.2 of Chapter 5, it has been necessary to evaluate the geometrical acceptance of the setup to detect cosmic muons. This way, a C++ Monte Carlo simulation has been written using the dimensions of the experimental setup. By running 1000 simulations in which a million muons were generated in a source plane much larger than the experimental setup itself to reach high zenith angles, the geometrical acceptance was measured to be (0.9835 ± 0.0014) . This factor has then been used to correct the measured efficiency of the detector.

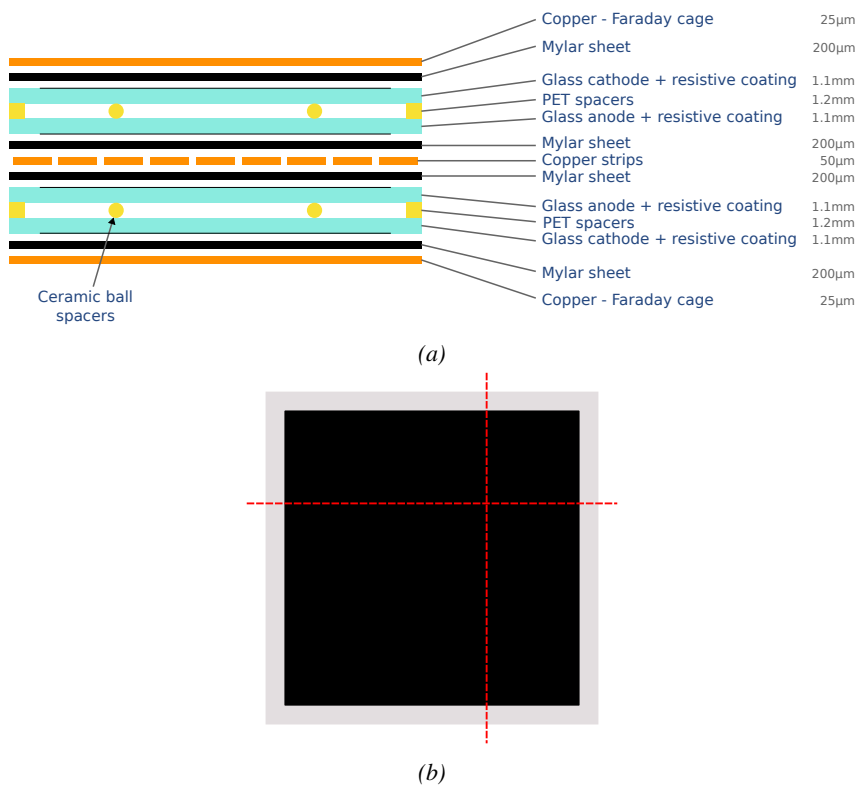


Figure 6.17: The glass RPC developed by Ghent uses a double-gap design (Figure 6.17a). The electrodes are made of four pieces of float glass glued into a single plate (Figure 6.17b). Indeed a gluing technique has been investigated as most new low resistivity materials foreseen for RPCs of the new generation are not available in large areas.

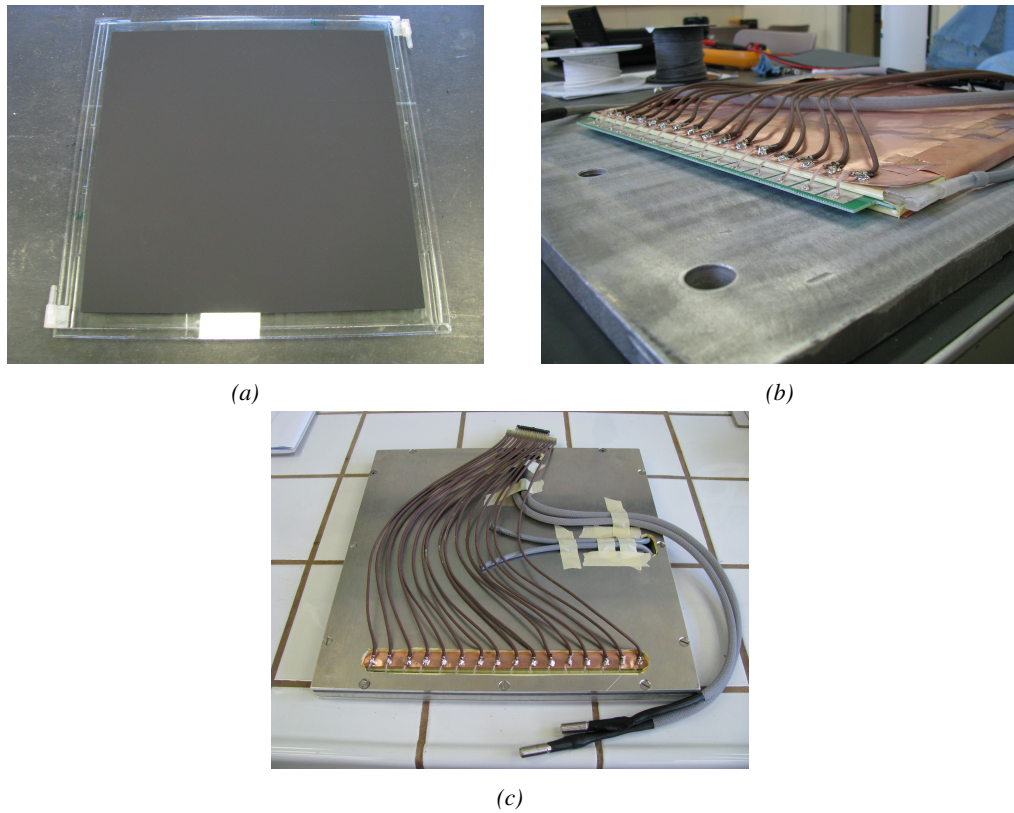


Figure 6.18: Figure 6.18a: A gap used to conceive the gRPC tested at CERN. Figure 6.18b: Both gaps with their read-out panel are placed into a faraday made out of copper. Figure 6.18c: The faraday cage containing the double-gap gRPC is finally placed into its aluminium case.

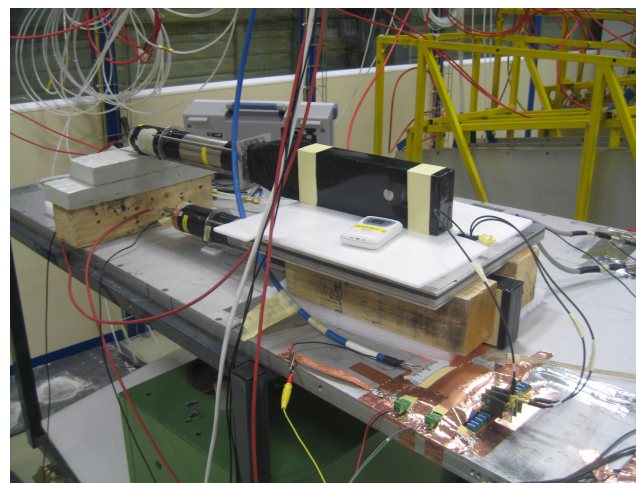


Figure 6.19: Experimental setup used to test the INFN preamplifier mounted on the CMS like FEB with the glass RPC build by Ghent.

4018 Thanks to the activities ongoing for the preparation of the CMS RPC experiment taking place
 4019 at GIF++ and detailed in Chapter 5, a first prototype of DAQ software was available to automate
 4020 the data tacking process. Thanks to this early version of the software, the pulse processing was
 4021 made more simple. The three channels connected to the preamplifiers were sent directly into a
 4022 V1190A TDC manufactured by CAEN. The trigger was provided by the same trigger pulse process-
 4023 ing described in Figure 6.15. The output of the coincidence of both scintillators was sent into the
 4024 *TRIGGER* input of the TDC. The communication with the computer was done thanks to a V1718
 4025 module. More details on the DAQ can be found in Appendix A. Contrary to the data now collected
 4026 at GIF++, the output of the first DAQ script consisted in a simple text file using a format described
 4027 in Source Code 6.1. The analysis is then performed using a loop through the data file.

```
4028   Evt0      nHits
    ChHit1    THit1
    ChHit2    THit2
    ChHit3    THit3
    ChHit4    THit4
    ChHit5    THit5
...
4029   Evt1      nHits
    ChHit1    THit1
    ChHit2    THit2
    ChHit3    THit3
...

```

Source Code 6.1: Description of the format used to store the data collected during the experiment aiming at testing the INFN electronics with a gRPC built by Ghent. For each trigger received in the TDC module, an event is created. A first line containing two columns is written in the output file with the event number `EvtX` and the recorded number of hits `nHits`. This line is directly followed by the list of hits in each channel `ChHitX` and their corresponding time stamp `THitX` organized into two columns.

4030 The results of the experiment with the gRPC are provided in Figure 6.20 and Table 6.3. The
 4031 efficiency of the detector reaches 95% at working voltage, indicating that such a detector using
 4032 electrodes composed of several glued pieces can be an option for the future of RPC technologies.
 4033 The benefits of the preamplifiers is once again visible through the huge efficiency shift towards lower
 4034 voltages. The shift reaches almost 470 V for thresholds lower than 6 fC.
 4035 The cluster size also shows a shift but its value suddenly decreases after 5.4 kV. After a rise above 2,
 4036 the cluster size drops when the detector reaches the plateau. A first idea to explain this phenomenon
 4037 would be to check the cluster algorithm to make sure that it is not biased and does not introduce
 4038 a fake split of the clusters due to arbitrarily strict selection rules. Clusters are always made of
 4039 neighbour strips getting a hit within a certain time window. In the algorithm written to analyse
 4040 the data, it is required for the maximum time difference between the earliest hit and the latest hit
 4041 in a cluster to be smaller than 10 ns. Physically, assuming of drift velocity of the electrons in the
 4042 gas of the order of 0.1 mm/ns [286], the growth of an avalanche only takes a few ns. This effect
 4043 is visible in Figure 6.21a in which the maximum time difference has been artificially increased to
 4044 300 ns. The peak reaveals that the avalanches are not expected to grow over a time period longer than
 4045 10 ns. No peak emerges at time differences longer than 10 ns indicating that the choice of a short
 4046 time development within the algorithm was justified. This conclusion is supported by Figure 6.21b
 4047 in which the evolution of the reconstructed cluster size with increasing maximum time difference
 4048 shows no effect.

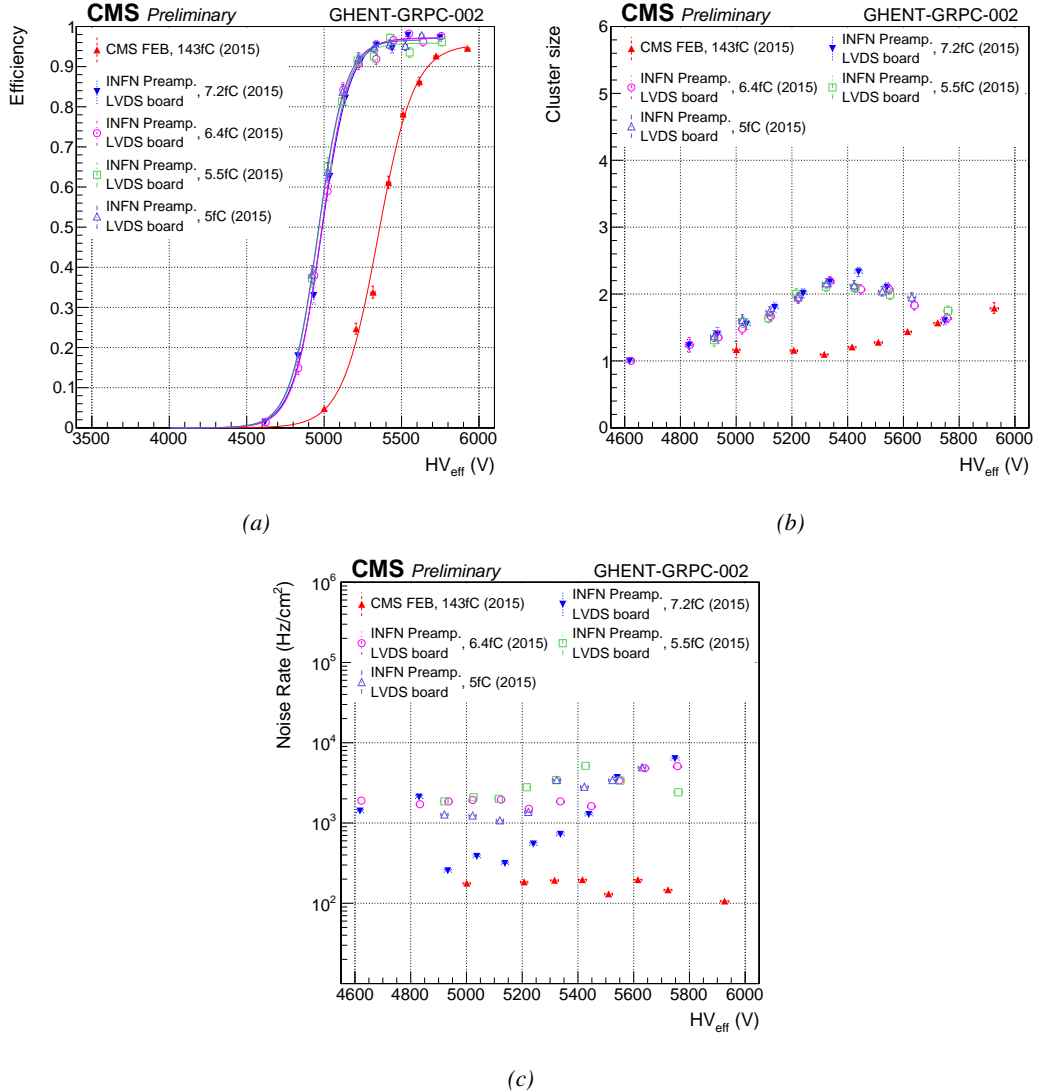


Figure 6.20: Efficiency (Figure 6.20a), cluster size (Figure 6.20b) and noise rate per unit area (Figure 6.20c) of the Ghent gRPC detector tested with the standard CMS FEBs (red) and with the INFN preamplifier mounted onto the CMS FEB at different thresholds (blue, pink, green and purple).

Data	ϵ_{max}	$\lambda \cdot 10^{-2} \text{ V}^{-1}$	HV_{50} (V)	ϵ_{WP}	HV_{WP} (V)
CMS FEB, 143fC (2015)	0.956 ± 0.007	0.86 ± 0.04	5349 ± 8	0.94 ± 0.01	5839 ± 23
INFN/CMS FEB, 7.2fC (2015)	0.972 ± 0.006	1.09 ± 0.06	4983 ± 8	0.96 ± 0.01	5403 ± 22
INFN/CMS FEB, 6.4fC (2015)	0.971 ± 0.005	1.13 ± 0.06	4981 ± 8	0.96 ± 0.01	5391 ± 22
INFN/CMS FEB, 5.5fC (2015)	0.959 ± 0.006	1.13 ± 0.11	4960 ± 11	0.95 ± 0.02	5371 ± 37
INFN/CMS FEB, 5fC (2015)	0.967 ± 0.006	1.12 ± 0.11	4959 ± 11	0.96 ± 0.02	5371 ± 38

Table 6.3: Results of the sigmoid fit (Formula 3.24) performed on the data presented in Figure 6.20a. The working point and its corresponding efficiency are computed using Formulas 3.24 and 3.25.

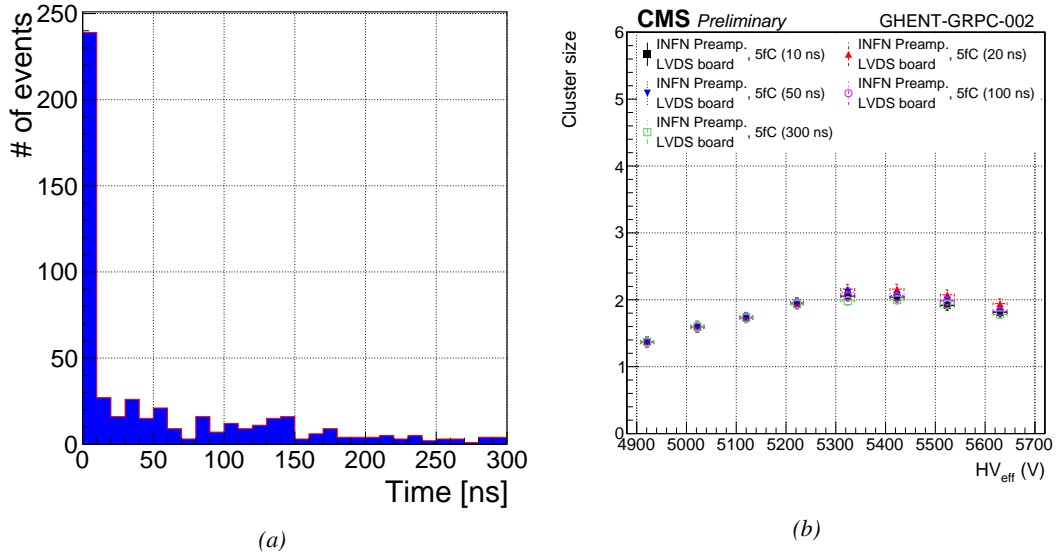


Figure 6.21: Figure 6.21a: Time difference between the first and last hit composing a cluster in the gRPC. The maximum time difference is set to 300 ns. Figure 6.21b: Variation of the reconstructed average cluster size as a function of the time constraint used in the algorithm.

4049 Due to the available number of channels, the cluster size is limited to 3. It is reasonable to
 4050 assume that this only is the cause of the fall of cluster size beyond 5.4 kV. Indeed looking closely at
 4051 both Figure 6.22 and Figure 6.23, the link between increasing HV and decreasing cluster size can be
 4052 understood. On the one hand, Figure 6.22 indicates that the cluster size features at first a maximum
 4053 at 1. The maximum moves then from 1 to 3 over the points at 5120 V, 5222 V and 5324 V. Then over
 4054 the last three voltage points, the bin at 2 drops to the profit of the bin at 1, the bin at 3 staying more
 4055 or less stable. On the other hand, Figure 6.23 provides us more information about the localisation of
 4056 the clusters among the three read-out strips. At the lowest two voltages, most of the data is contained
 4057 in the central strip. At 5120 V, the highest bin is the one corresponding to the central strip with a
 4058 cluster size of 1. Already at 5222 V, the balance changes towards the central strip with 3 strips in
 4059 the clusters. At 5324 V, even more events happen with clusters of all 3 strips while the events with
 4060 a single hit in the side strips starts to increase. The number of events with cluster made of all 3
 4061 strips will not vary much anymore while the number of events with clusters made of 2 strips will
 4062 decrease and the single hits in the side strips will continue rising. This information indicates that
 4063 the avalanches in the gap start to get stronger. Indeed, the increase of the events containing single
 4064 hits mainly increases on the side strips points to an intensification of the avalanche gain on the strip
 4065 adjacent to the three channels connected to the read-out setup. Only a single hit is read-out while
 4066 in reality this was the contribution of bigger avalanches. The events with clusters of size 2 tend to
 4067 decrease due to the stronger gain that should normally be triggering wider avalanches. The cluster
 4068 size distribution of Figure 6.22 gives the impression that the distribution is moving towards higher
 4069 values but the geometrical limitation of the system due to the very low number of channels makes it
 4070 impossible to measure.

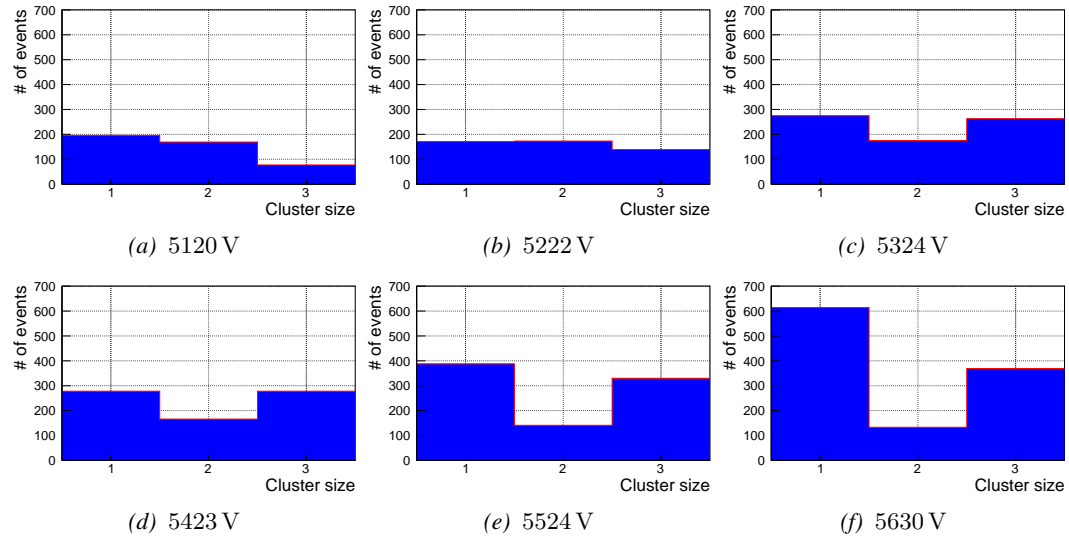


Figure 6.22: Evolution of the cluster size distribution with increasing voltage for the gRPC tested with the INFN preamplifiers using a threshold of 5 fC.

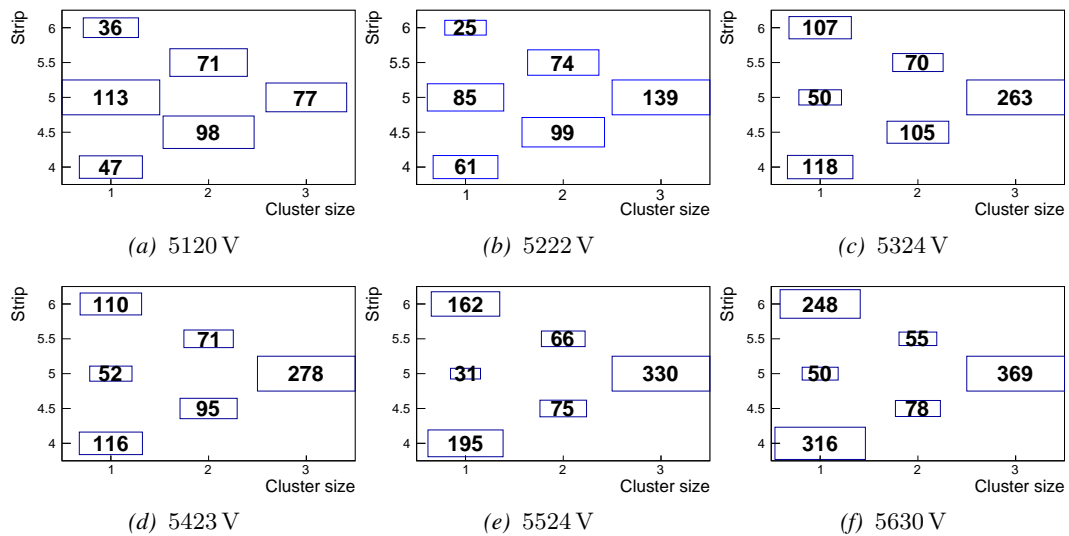


Figure 6.23: Map of the cluster size distribution as a function of the cluster position with increasing voltage for the gRPC tested with the INFN preamplifiers using a threshold of 5 fC.

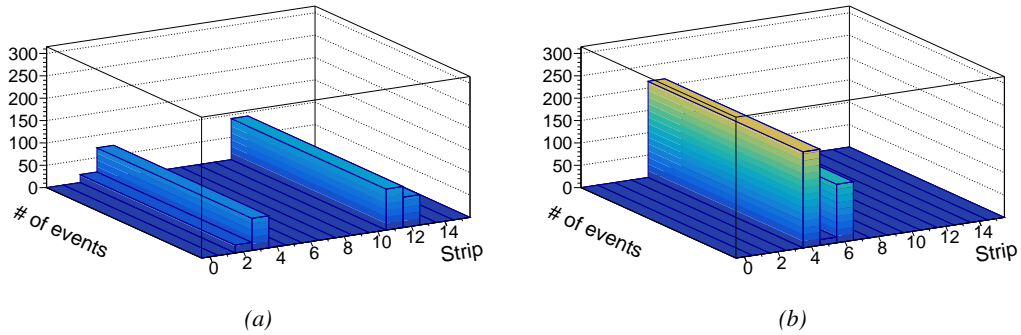


Figure 6.24: Noise profile measured in the glass RPC built by Ghent tested with the standard CMS FEB (Figure 6.24a) and the INFN preamplifiers mounted on a CMS-like FEB (Figure 6.24b).

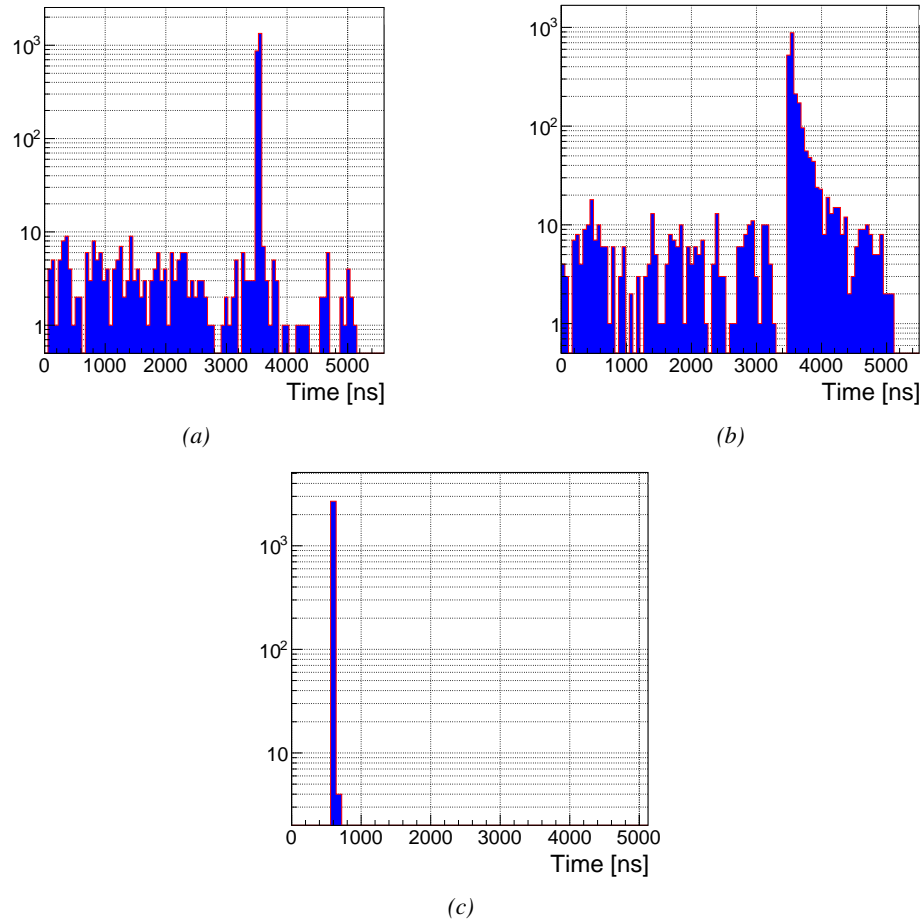


Figure 6.25: The arrival time of the hits recorded in the gRPC tested with the CMS FEB (Figure 6.25a) and with the INFN preamplifiers (Figure 6.25b), and recorded in the CMS RE2 RPC tested with the INFN preamplifiers (Figure 6.25c).

Eventhough the performance of the detector are promising, the results concerning the noise rate per unit area seem to indicate that the detector and its combination with the electronics in the case of this experiment produces very high levels of noise, if compared to the noise measured in the RE4 detector. With each type of electronics, the noise doesn't indicate a clear correlation with increasing voltage. The hypothesis at this stage would be that the noise is not created inside of the gas volume by avalanches triggered along the glueing lines, where the electric field could be abruptly pertubated. It would rather come from the read-out channel itself, and from its connection to the electronics. Indeed, looking at the noise profile measured in the detector and presented in Figure 6.24a, it is clear that the noise is localised in two areas corresponding to the HV connectors in the case of the HV scan performed with the CMS FEB. Moreover, contrary to the very careful work performed on the RE2 chamber to match the impedance of the strips with the read-out cables connected to the board on which the INFN preamplifiers are mounted, no matching was done on the gRPC due to a lack of time. The noise measured in the tested three channels is showed in Figure 6.24b. This region of the detector doesn't correpond to the HV connectors according to Figure 6.24a. Nevertheless, the number of hits counted in the detector is much higher than in the CMS FEB case. Looking more carefully to Figure 6.25 presenting the hit time profile in both cases together with the time profile of the CMS RE2-2 detector tested with INFN preamplifiers, it is clear that the detector is noisier. Also, the reflections due to the impedance mismatch is clearly visible in Figure 6.25b.

6.2.3 HARDROC 2 based RPC read-out

The HAdronic RPC Digital Read-Out Chip (HARDROC) ASIC, as its name suggests, has been developped for RPC applications and in particular for the read-out RPCs of the SDHCAL that is being studied in the perspective of the International Linear Collider (ILC). The SDHCAL detectors are required to have a high granularity compared to the CMS RPCs and hence, they use 1 cm^2 read-out pads instead of strips. This choice results in a huge number of channels. The ASIC is mounted directly on the read-out pannel for compactness as can be seen in Figure 6.26a and feature three thresholds to provide a semi-digital information.



Figure 6.26: Experimental setups used to test the HARDROC2 electronics with a CMS RE4-3 gap (Figure 6.26a) and a gRPC gap built in Ghent (Figure 6.26b).

The PETIROC that inspired the CMS RPCROC uses a similar technology than the one developed for the HARDROC and is manufactured by the same company. It is safe to conclude that the preliminary results obtained with the HARDROC electronics constitute a strong indication on

4100 the potential performance of a FEB developped specifically for CMS detectors. The leading institute
 4101 in the development of the SDHCAL based on single-gap glass RPCs (gRPCs) is the Institut de
 4102 Physique Nucléaire de Lyon (IPNL) which also played a great role in developing iRPCs for CMS.

4103 A read-out pannel using the HARDROC 2 technol-
 4104 ogy was lended by this institute and was tested onto a
 4105 CMS RPC. Contrary to the tests with the INFN pream-
 4106 plifiers that were made using an RE2-2 CMS RPC built
 4107 in 2007 for the second endcap disk of CMS, the choice
 4108 was made to use an RE4-3 detector built during LS1 to
 4109 equip the fourth endcap. Indeed, the pannel can't be
 4110 sandwiched between two RPC gaps due to the embed-
 4111 ded electronics and a single CMS RPC gap was used.
 4112 At the time of this experiment, only RE4-3 gaps were
 4113 available and the choice was made to change detector
 4114 with respect to the previous series of tests conducted on
 4115 the INFN preamplifiers. As for the INFN preamplifiers,
 4116 the pannel has been tested on the gRPC built by UGent.
 4117 The gRPC being smaller than the HARDROC read-out
 4118 that was used for the experiment but thanks to the 2D
 4119 read-out using pads, this was not a problem for the data
 4120 acquisition.

4121 Once again, the experiment was conducted in the
 4122 CMS RPC assembly laboratory at CERN and the setups are shown in Figure 6.26. The read-out
 4123 panel is placed directly on top of the gaps and pressed against the detector surface thanks to weights.
 4124 The same PMTs are used to provide a trigger to the data acquisition. In the particular case of the
 4125 HARDROC 2 electronics, the output signal does not correspond to the LVDS signals provided by
 4126 the CMS FEB. Moreover, there would be more than 1500 channels to constantly monitor and unfor-
 4127 tunately, there would not be enough VME TDC modules to use with the DAQ software designed for
 4128 the experiment involving the INFN preamplifiers. Nevertheless, a custom-made DAQ software was
 4129 designed by the members of IPNL's team to read-out the electronics through the chip presented in
 4130 Figure 6.27. The data is stored in the buffer of the ASIC continuously and dumped into the computer
 4131 when a trigger signal is received.

4132 The results of the tests conducted with the HARDROC 2 on a CMS gap are presented in Fig-
 4133 ure 6.28 and Table 6.4. These results can hardly be compared to what was measured with the INFN
 4134 preamplifiers as the detector was not tested using the single-gap mode. The tested thresholds are high
 4135 compared to the ones displayed by the INFN preamplifiers and are of the order of magnitude of the
 4136 current CMS FEB. Nevertheless, the performance of the detector equipped with this read-out pannel
 4137 is measured to be better. Indeed, a shift of 400 to 500 V is observed at thresholds ranging from 230
 4138 to 121.4 fC. *This could be explained by the difference in read-out channel areas of both read-out*
4139 panels. Indeed, in the case of the standard CMS RPC, the read-out panel consists in relatively large
4140 trapezoidal strips when the read-out of the HARDROC 2 is composed of 1 cm² pads. Due to the
4141 cross-talk between adjacent channels, the charge produced by a growing avalanche is spread over a
4142 larger surface in the case of the standard CMS RPC, leading to a smaller signal relative to the pads.
[This is only I idea to explain this phenomenon for now. It needs cross check. If approved, I
4143 would need to quantify the expected difference.]

4144 The cluster size is provided for information as a direct comparison of the cluster size measured with
 4145 1 cm² pads and long copper strips with width of a few cm is not possible. The measured cluster size
 4146 at working voltage with the CMS FEB is consistent with what would be expected of a single-gap
 4147 RPC. Indeed, the usage of two gaps in an OR system allows for a stronger overall gain and hence,



Figure 6.27: HARDROC2 control chip with its "Mezzanine" used to collect the data from the different HARDROC ASICs and communicate with the computer. On top of the picture, the trigger is brought by a coaxial cable. The connection with the computer is assured by both the USB cables.

4149 the cluster size is greater. A more precise estimation of the charge spread inside of the gap is ob-
 4150 tained using pads instead of strips. At working voltage, an avalanche is detected within less than
 4151 two pads on average. An extra information could be used to further improve the spatial resolution of
 4152 the detector. Indeed, as stated in the introduction of the Section, the HARDROC 2 is a semi-digital
 4153 electronics and features three threshold levels. Tuning these thresholds would lead to an approxi-
 4154 mation of the induced charge profile over the neighbouring pads. A gaussian fit over the digitized
 4155 distribution would give an estimation of the position of the avalanche center.

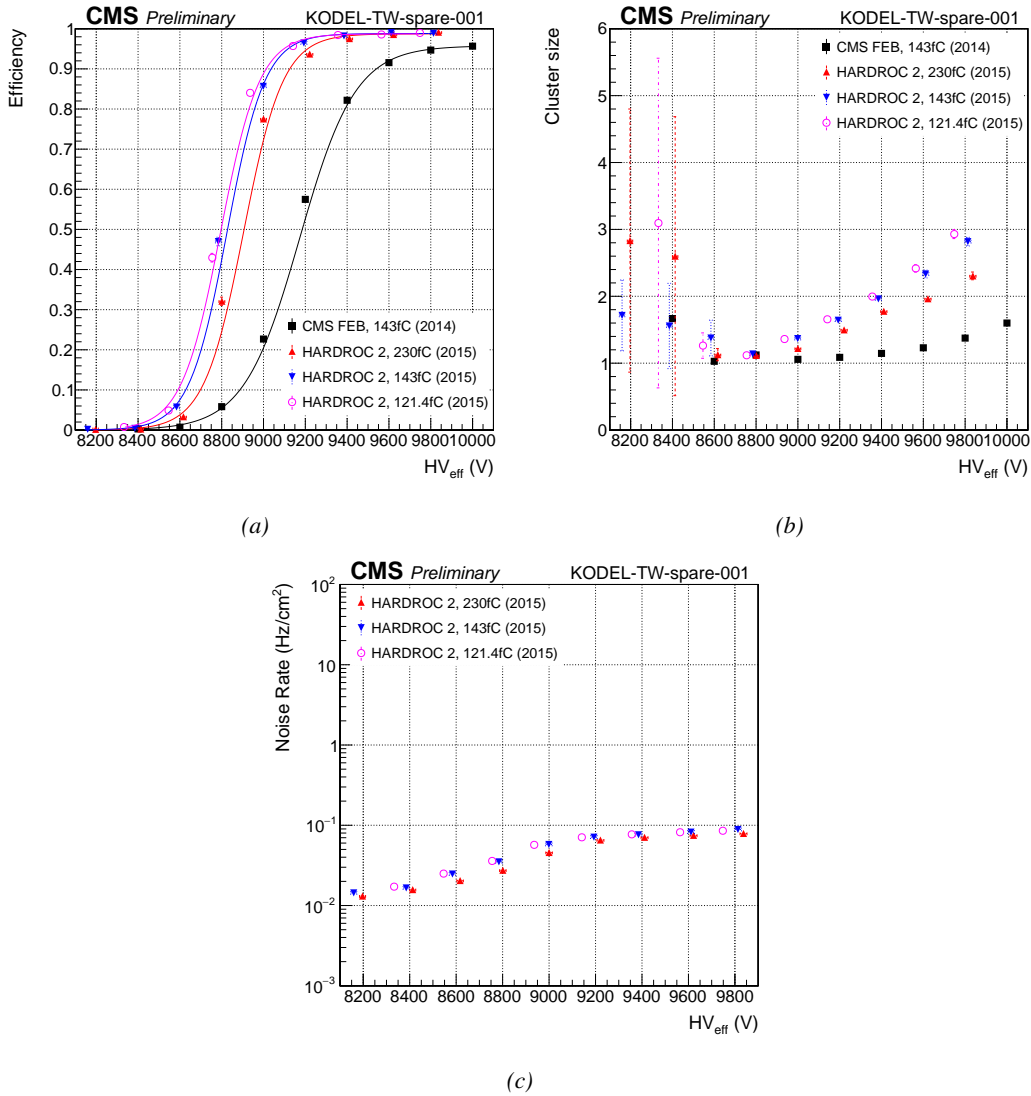


Figure 6.28: Efficiency (Figure 6.28a), cluster size (Figure 6.28b) and noise rate per unit area (Figure 6.28c) of the CMS RE4-3 detector tested in single gap mode with the standard CMS FEBs (black) and with the HARDROC 2 readout panel at different thresholds (red, blue and pink).

Data	ϵ_{max}	$\lambda \cdot 10^{-2} \text{ V}^{-1}$	$HV_{50} (\text{V})$	ϵ_{WP}	$HV_{WP} (\text{V})$
CMS FEB, 143fC (2014)	0.958 ± 0.000	0.75 ± 0.00	9174 ± 1	0.94 ± 0.00	9716 ± 2
HARDROC 2, 230fC (2015)	0.987 ± 0.002	1.06 ± 0.04	8905 ± 8	0.98 ± 0.01	9333 ± 17
HARDROC 2, 143fC (2015)	0.988 ± 0.001	1.10 ± 0.04	8826 ± 8	0.98 ± 0.01	9243 ± 17
HARDROC 2, 121.4fC (2015)	0.987 ± 0.001	1.07 ± 0.04	8795 ± 8	0.98 ± 0.01	9220 ± 17

Table 6.4: Results of the sigmoid fit (Formula 3.24) performed on the data presented in Figure 6.28a. The working point and its corresponding efficiency are computed using Formulas 3.24 and 3.25.

Finally, the noise measured in the electronics is of the same order of what had been measured in Figure 6.16c. It is safe to assume that the noise level in the case of a single-gap RPC is expected to be of the same order of magnitude than its double-gap counterpart as the noise mainly is electromagnetic. Figure 6.29 provides a clearer understanding of the position of the trigger PMTs and of the noise measured with the HARDROC. The noise of the electronics itself is very small and the read-out pannel is sensitive enough to measure the noise in the RPC gap. Indeed, except for a few visible hot spots, the observed noise profile corresponds perfectly to the spacer positions inside of the gap volume. The PET buttons used to maintain the uniformity of the gas volume cause noise at their proximity as they modify the local electric field.

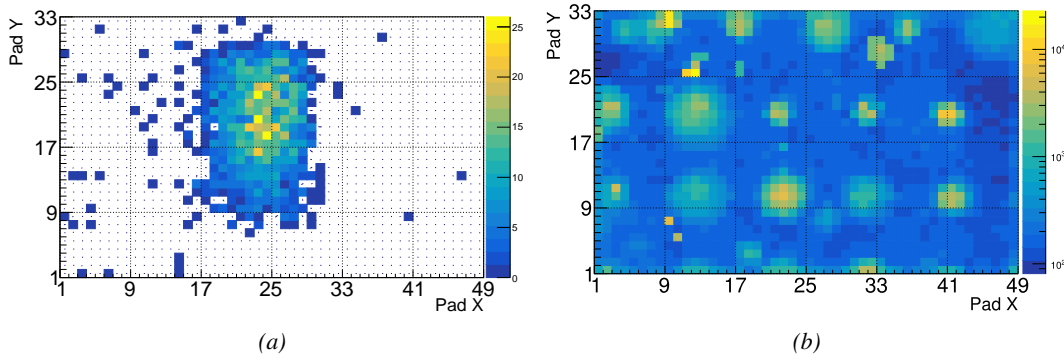


Figure 6.29: Measured muon (Figure 6.29a) and noise (Figure 6.29b) profiles in the read-out pads of the HARDROC 2 over a CMS RE4-3 gap. The inner structure of the gap and the presence of the spacers in the volume is visible.

The results of the experiment with the gRPC are provided in Figure 6.30 and Table 6.5. Unfortunately the gRPC had not been tested in single gap mode with the CMS FEB. Thus, a direct comparison is not possible as the data were not collected in similar conditions. The detector could only be tested with a single HARDROC 2 threshold setting (143 fC). As for the double-gap, the efficiency of the single-gap reaches 95% at working voltage. The working voltage is consistent with the double-gap detector operated with the CMS FEB indicating that the HARDROC is more sensitive to lower charges. The difference in efficiency rising is consistent with the use of one gap versus two in the case of the CMS FEB.

As discussed in the case of the CMS RE4-3 gap, the direct comparison of the cluster sizes is not possible. In this sense, the proximity of both results only is fortuitous. The cluster size of approximately 1.6 measured with the HARDROC 2 at working voltage is of the same order than what had previously been measured for the CMS gap indicating that at equivalent performance, the gain and hence, the induced charge could be comparable.

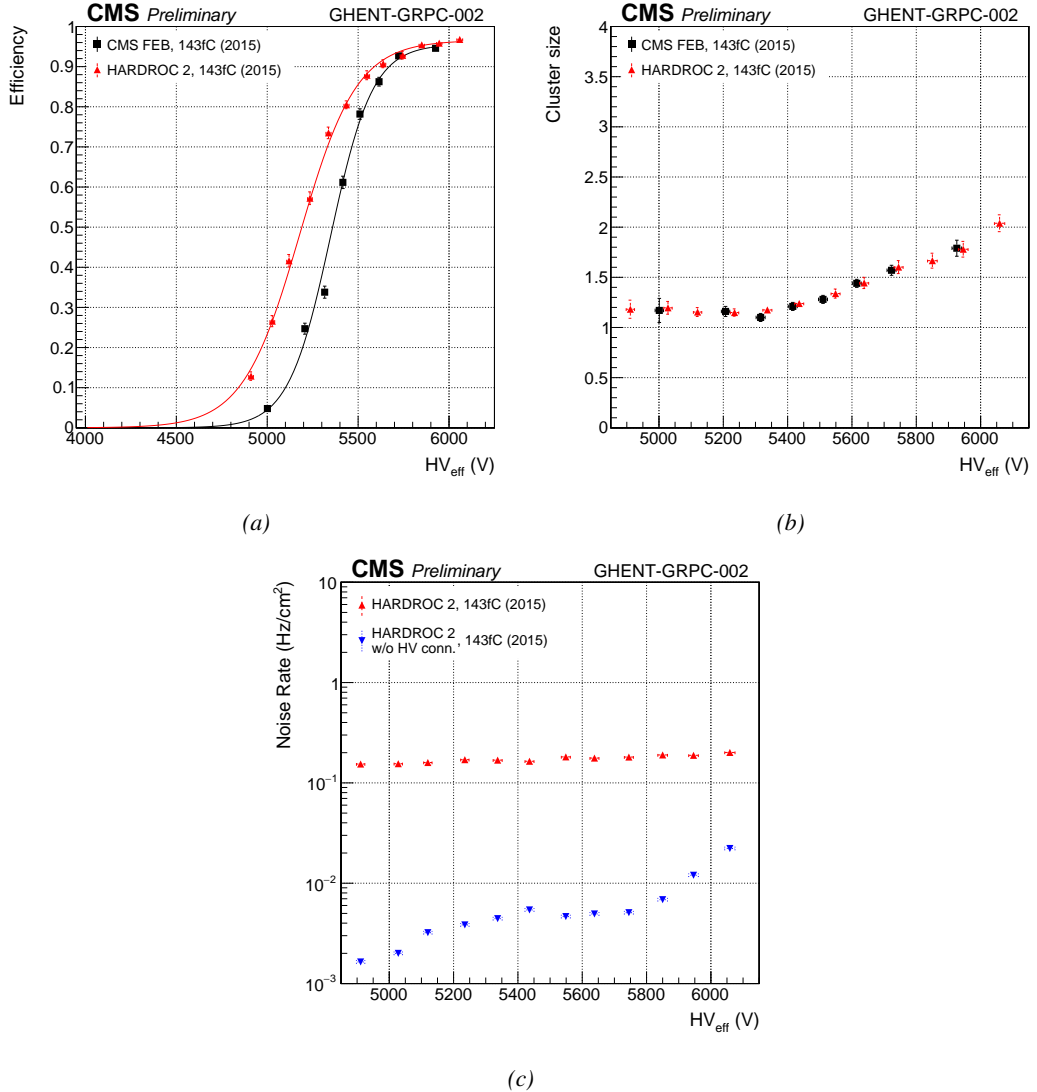


Figure 6.30: Efficiency (Figure 6.28a), cluster size (Figure 6.28b) and noise rate per unit area (Figure 6.28c) of the UGent gRPC tested in double-gap mode with the standard CMS FEBs (black) and in single-gap with the HARDROC 2 readout panel at a threshold of 143 fC (red).

Data	ϵ_{max}	$\lambda \cdot 10^{-2} \text{ V}^{-1}$	HV_{50} (V)	ϵ_{WP}	HV_{WP} (V)
CMS FEB, 143fC (2015)	0.956 ± 0.007	0.86 ± 0.04	5349 ± 8	0.94 ± 0.01	5839 ± 23
HARDROC 2, 143fC (2015)	0.966 ± 0.004	0.64 ± 0.02	5179 ± 7	0.95 ± 0.01	5790 ± 25

Table 6.5: Results of the sigmoid fit (Formula 3.24) performed on the data presented in Figure 6.30a. The working point and its corresponding efficiency are computed using Formulas 3.24 and 3.25.

Finally, the noise measured in the electronics seemed higher than in the case of the CMS gap. Looking closer to the noise profile provided in Figure 6.31, it can be seen that the noise measurement was affected by the HV connector. Indeed, the high noise measured in pads 41 and 42 along X and 22

to 25 along Y, corresponds exactly to the position of the HV connector on the cathode side. Contrary to the case of the CMS gap were the HV connector was far from the read-out area, the gRPC is smaller than the read-out and due to the poor grounding of the setup the electric field created by the HV connector could affect the read-out. Excluding the corresponding pads gives a much more reliable noise measurement as can be seen in Figure 6.30c. Through the noise profile, a better understanding of the gRPC uniformity can be obtained. First of all, the row corresponding to Y=16 seem consistently noisier than the neighbouring pads and could correspond to the glueing line that lies along this pad row. The noise increase along this line is not very clear though and no corresponding behaviour can be observed along the other glueing line along column X=30. But the gas volume corresponding to the largest glass plate, spreading from columns 31 to 47 along X and rows 1 to 15 clearly shows a stronger noise in its center. The detection area being small, only a few ceramic ball spacers were used to maintain the distance in between the electrodes. It is not impossible that the ball spacer located in the center of this very volume popped out. Due to the absence of a spacer, the force applied by electric field onto the electrodes could have made the distance in between the electrodes smaller and artificially increased the observed electric field, also increasing the measured noise.

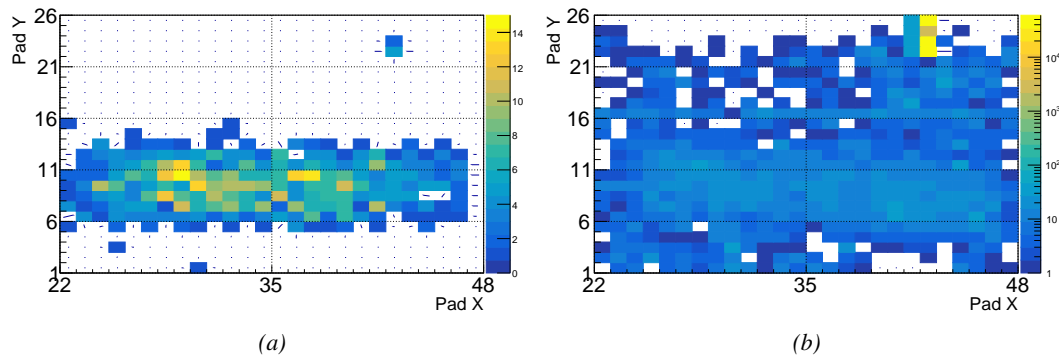


Figure 6.31: Measured muon (Figure 6.31a) and noise (Figure 6.31a) profiles in the read-out pads of the HARDROC 2 over a gRPC gap built by Ghent.

6.3 Outlook on the current FEE certification status

In this Section will be presented the ongoing certification of the CMS RPCROC and of the INFN Tor Vergata FEBs chosen as back-up solution. For reference, an iRPC has been operated without irradiation with the standard CMS FEB. It is reminded that the iRPCs that will complete the redundancy of the muon system of CMS close to the beam line are expected to suffer a background hit rate per unit area of 600 Hz/cm². Including a safety factor of 3, it is then necessary for the detectors to be certified at a minimal background hit rate of 2 kHz/cm².

6.3.1 CMS Front-End Board reference

The iRPCs that will be installed at CMS will be equipped with new Front-End Electronics. Nevertheless, in order to compare the performance of the new electronics with the standard CMS FEBs, a series of short characterization tests was carried out with an iRPC prototype. Seven strips of a read-out panel designed for a back-up scenario detector were connected to a CMS FEB. The remaining strips were connected to the ground to avoid noise. The tests were done without irradiation and using cosmic muons. Two narrow scintillators were placed on each side of the prototype to provide a trigger signal as can be seen from Figure 6.32. The tests were performed with three detection thresholds

⁴²¹¹ of 200 mV (\approx 133 fC), 210 mV (\approx 140 fC) and 220 mV (\approx 146 fC) on the FEB discriminators. The
⁴²¹² LVDS output of the FEB was then read-out with a CAEN TDC.



Figure 6.32: Experimental setup used to test the iRPC equipped with the standard CMS FEEs. Seven of the 96 strips are connected to the read-out channels.

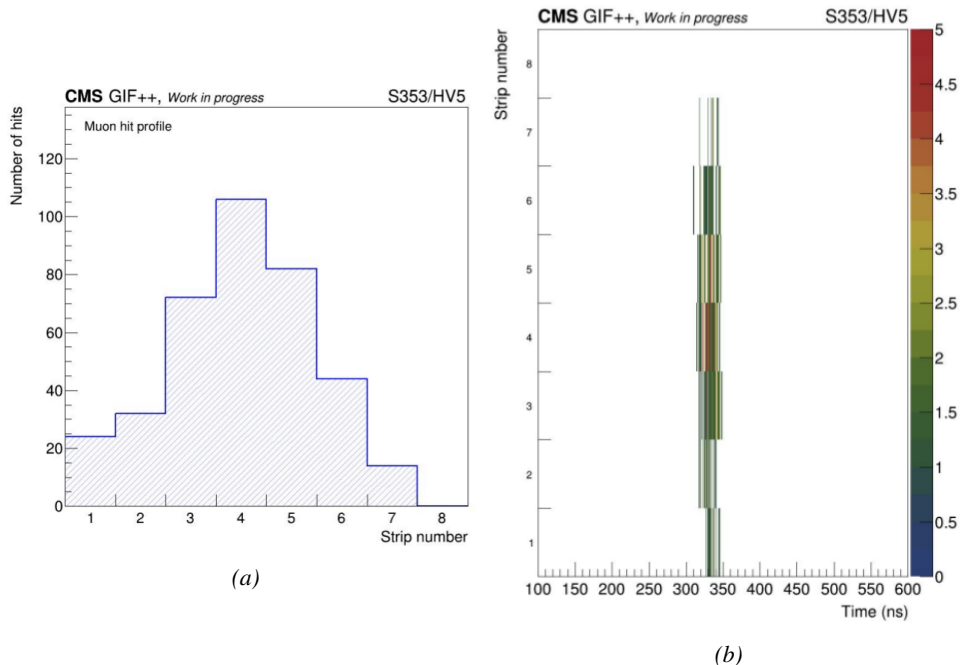


Figure 6.33: (a) Distribution of the muon hits on the seven strips connected to the standard CMS FEB. Strip 8 is connected to the ground. (b) Time distribution of the hits in the seven channels. The color scale corresponds to the number of hits per bin.

⁴²¹³ The HV scans consisted of seven effective voltage steps (6800, 7000, 7100, 7200, 7300, 7400
⁴²¹⁴ and 7500 V) at which 100 muon triggers were requested as minimal statistics. The hit profile over the
⁴²¹⁵ connected strips as well as the time profile of the events in each channel is provided in Figure 6.33
⁴²¹⁶ for the fifth HV step (7300 HV). The area covered by the trigger is seen to be comparable than the
⁴²¹⁷ width of the seven strips. The time arrival of the hits is well confined within less than 50 ns.

The results for this kind of electronics are to be found in Figure 6.34. First of all, the efficiency at working voltage of the detector reaches 96.9% at a threshold of 146 fC, 97.0% at 140 fC and finally 96.6% at 133 fC. The efficiency does not seem to be affected by a change of threshold. The working voltage, on the other hand, is shifted towards lower effective voltage values with decreasing threshold. The values of working voltages respectively are 7552, 7473 and 7393 V. This is expected by the lower gain necessary to produce large enough avalanches. No other differences can be observed at the level of the mean muon cluster sizes, mean muon cluster multiplicity per event and noise rate per unit area. The mean muon cluster size stays of the order of 2.4 strips per cluster and the muon cluster multiplicity, which is the number of reconstructed muon clusters per event, is consistent with 1 as expected. Finally, the noise rate per unit area is below 1 Hz/cm². The results are summarized in Table 6.6.

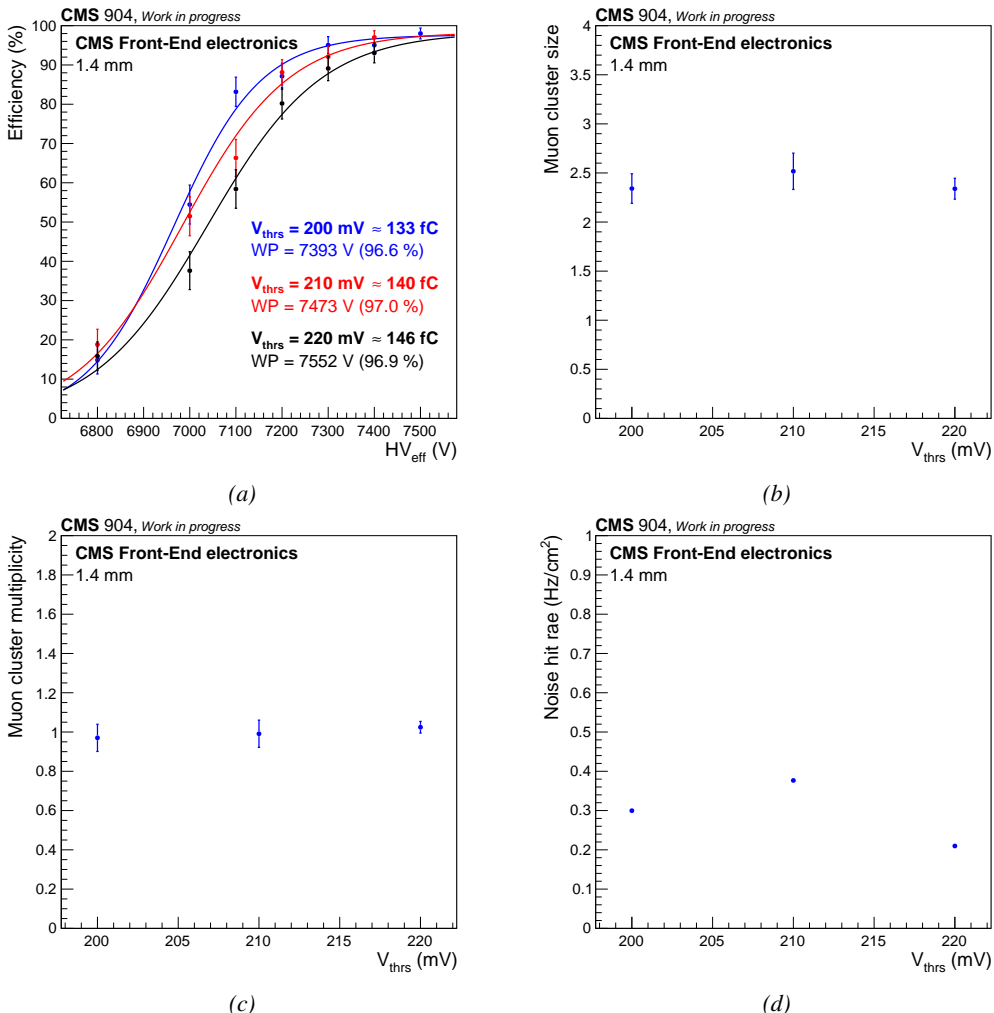


Figure 6.34: Summary of the HV scans performed on the iRPC prototype equipped with a standard CMS FEB at three detection thresholds. (a) Efficiency sigmoids. (b) Mean muon cluster size at working voltage. (c) Mean muon cluster multiplicity at working voltage. (d) Noise hit rate per unit area at working voltage.

Threshold (fC)	Working Voltage (V)	Efficiency (%)	Cluster Size	Multiplicity	Noise (Hz/cm ²)
146	7552 \pm 57	96.6 \pm 1.8	2.34 \pm 0.11	1.02 \pm 0.03	0.21
140	7473 \pm 49	97.0 \pm 2.5	2.52 \pm 0.18	0.99 \pm 0.07	0.38
133	7393 \pm 45	96.9 \pm 3.0	2.34 \pm 0.15	0.97 \pm 0.07	0.30

Table 6.6: Summary results of the iRPC operated with a standard CMS RPC FEB.

6.3.2 CMS RPCROC



Figure 6.35: Experimental setup used along the H2 muon beam at CERN to measure the linearity between beam position along the strip length and the time difference measured between both strip ends with the version 0 of the RPCROC.

knowledge of the position of the beam.

Several iRPCs equipped with different versions of RPCROCs have been assembled and tested. This process helped identifying the weaknesses of the FEEs and propose new improved versions. The last piece of the R&D process will be the FEBv2 equipped with three PETIROC 2C ASICs, three Cyclone V FPGAs hosting the TDCs, and a fourth FPGA to communicate with the back-end electronics.

In a first series of tests performed along the muon beam line H2 at CERN, the FEBv0 was certified for time resolution performances and linearity between the time difference of recorded muon signals measured at both strip ends and the beam position along the strip length. The experimental setup is shown in Figure 6.35 on which two iRPCs are placed between two narrow scintillators for a precise

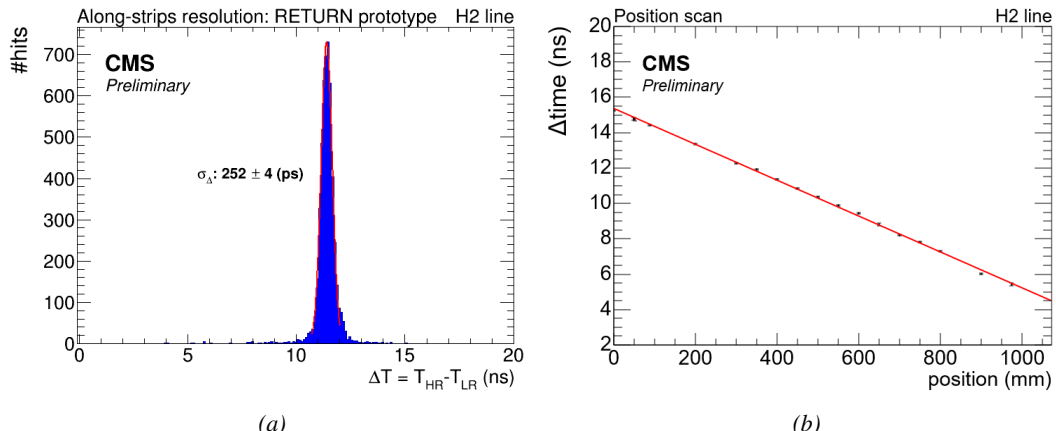


Figure 6.36: (a) Average time resolution of the iRPC equipped with an RPCROC FEBv0. (b) Linearity between reconstructed beam position along the strip length and the time difference measured between both strip ends.

$$(6.1) \quad \begin{aligned} Y &= \frac{L}{2} - \frac{v}{2} \times (T_{HR} - T_{LR}) \\ \Delta Y &= \frac{v}{2} \times \Delta(T_{HR} - T_{LR}) \end{aligned}$$

4249 The mean time difference between the signals measured at the high-radius (HR) and low-radius
 4250 (LR) is given in Figure 6.36a. The time resolution of the measurement is of (252 ± 4) ps. The velocity
 4251 of propagation v of the signals along the strips was reported to be of 1 m per 5.25 ns. According to
 4252 Equation 6.1, in which L is the length of the strip, Y the position along the strip, and T_{HR} and T_{LR}
 4253 the measured arrival time at the high-radius and low-radius ends of the strip, the spatial resolution
 4254 ΔY along the strip is then of the order of 2 cm. The linearity between the time difference and the
 4255 position of a hit along the strip length could then be studied with a good precision as can be seen in
 4256 Figure 6.36b.

4257 Later on, a new iRPC was assembled with FEBv1 using first PETIROC 2A. This version is re-
 4258 ferred to as FEBv1.1a. Due to a large cross-talk limiting the detection to 100 fC, the PETIROC 2A
 4259 was replaced by the PETIROC 2B. The lower threshold for stable operation of the FEBv1.1b could
 4260 be decreased to (50 ± 10) fC. However, operation of the detector with lower thresholds (≈ 26 10fC)
 4261 showed that part of the cross-talk could not be suppressed.

4262 The iRPC with FEBv1.1b was installed at the GIF++ as can be seen in Figure 6.37. The detector is
 4263 placed along the muon beam line and irradiated by the Cesium source. The results are displayed in
 4264 Figure 6.38. In each plot, the detectors were respectively (a) not irradiated, (b) irradiated to a back-
 4265 ground rate per unit area of (1.94 ± 0.25) kHz/cm², and (c) irradiated to a background rate per unit
 4266 area of (3.0 ± 0.5) kHz/cm².

4267 Without irradiation, the detector operated with detection threshold of (50 ± 10) fC reached its work-
 4268 ing voltage approximatively 140 V before the iRPC operated with the standard CMS FEB set to a
 4269 threshold of 133 fC. The efficiency at working voltage was of 97.4%, comparable to the efficiency
 4270 with the standard electronics.

4271 Near the certification background rate of 2 kHz/cm², the detector's working voltage was shifted
 4272 of almost 100 V and its efficiency decreased to 95.2%, demonstrating the good performance of the
 4273 detector. When irradiated at 3 kHz/cm², the detectors working voltage was not shifted any further
 4274 but its working efficiency had dropped to 92.5%.

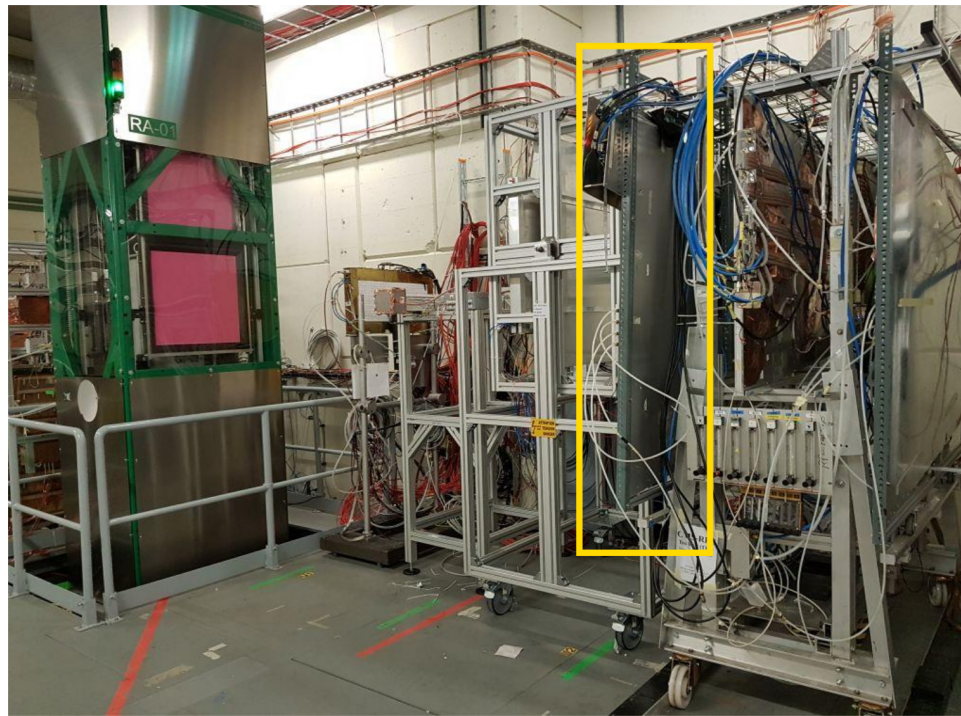


Figure 6.37: Experimental setup used at the GIF++ to certify the iRPC equipped with the RPCROC version 1. The chamber is placed along the beam line in front the Cesium source.

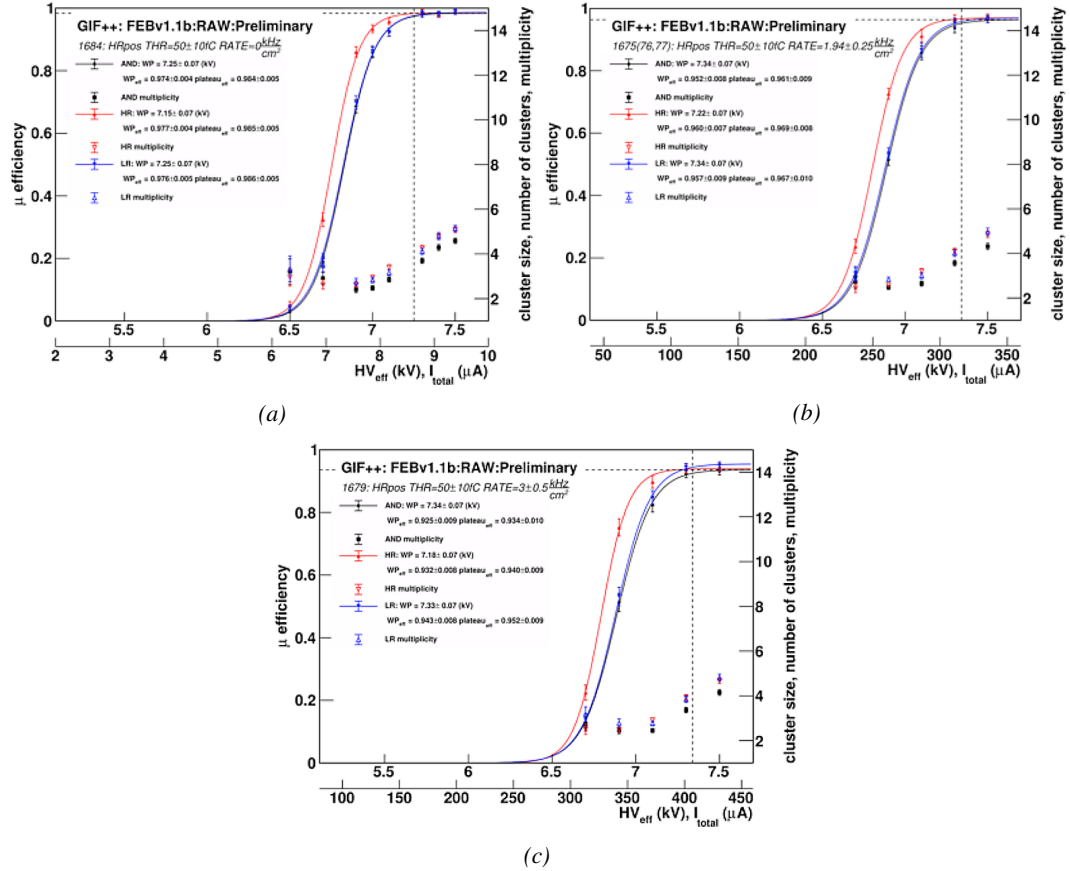


Figure 6.38: Efficiency scans obtained with the iRPC equipped with FEBv1.1b at the GIF++ (a) without irradiation, (b) for an irradiation of $(1.94 \pm 0.25) \text{ kHz/cm}^2$, and (c) for an irradiation of $(3.0 \pm 0.5) \text{ kHz/cm}^2$.

Hit Rate (kHz/cm ²)	Working Voltage (kV)	Efficiency (%)
0	7.25 ± 0.07	97.4 ± 0.4
1.94 ± 0.25	7.34 ± 0.07	95.2 ± 0.8
3.0 ± 0.5	7.34 ± 0.07	92.5 ± 0.9

Table 6.7: Summary results of the iRPC operated with a RPCROC FEBv1.1b set at a threshold of $(50 \pm 10) \text{ fC}$.

4275 6.3.3 INFN FEE

4276 An iRPC prototype equipped with the INFN Tor Vergata FEBs and a longitudinal read-out panel
 4277 alone was placed at the GIF++ for certification purposes. The chamber was tested for different
 4278 irradiation values.

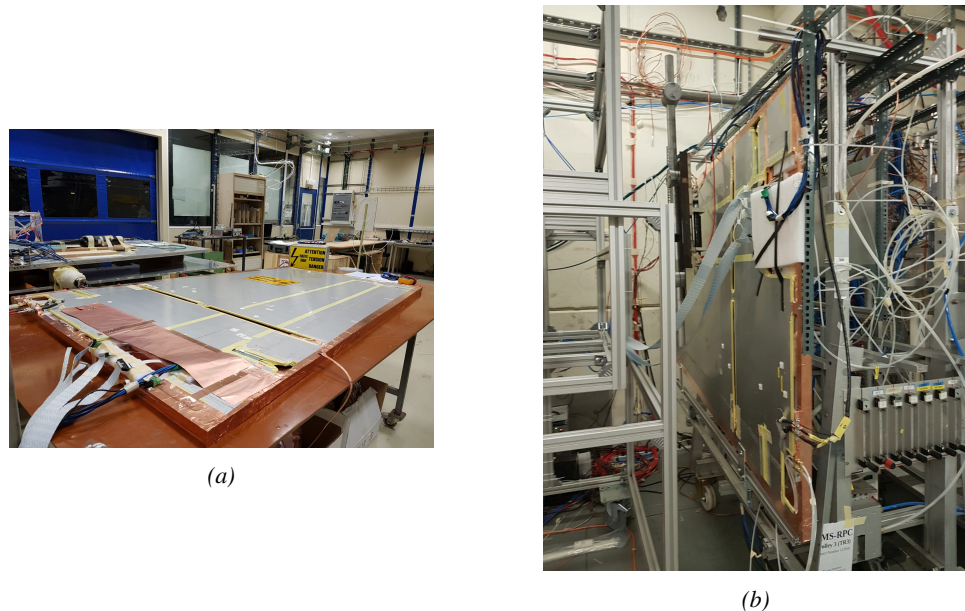


Figure 6.39: (a) iRPC prototype equipped with INFN Tor Vergata FEBs. The iRPC is enclosed in a spare RE1/3 case. The dimensions of the RE3/I and RE4/I iRPCs is in fact much smaller. (b) Experimental setup used at the GIF++ to certify the iRPC equipped with the INFN Tor Vergata FEB. The detector is in the beam line in front of the Cesium source.

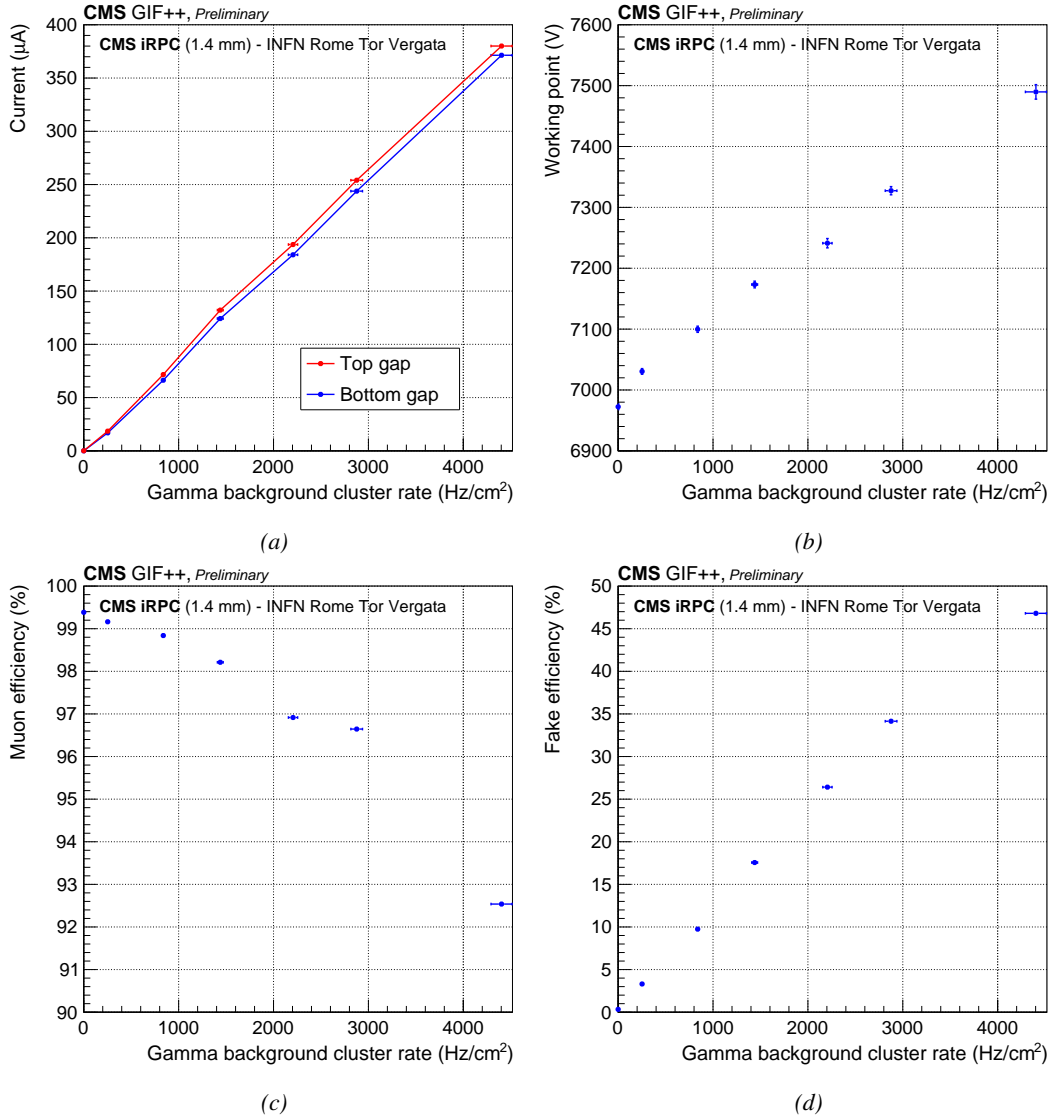


Figure 6.40

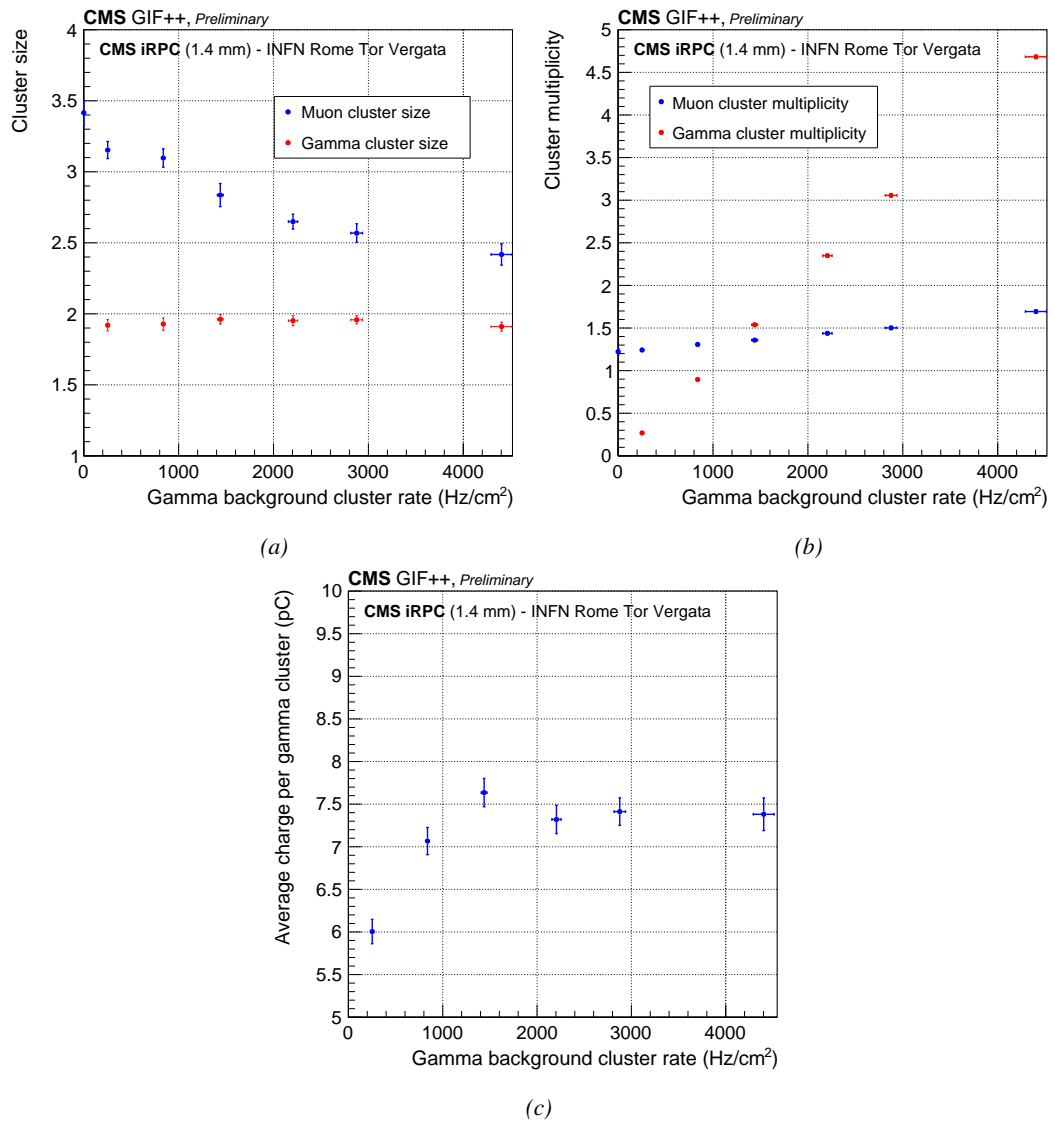


Figure 6.41